MASTER THESIS

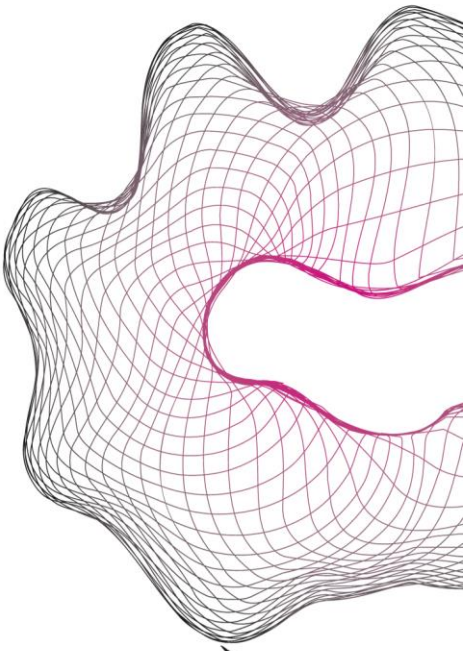

SCALING RULES FOR MICROROBOTS WITH FULL ENERGETIC AUTONOMY

Erwin van Renselaar

FACULTY OF ENGINEERING TECHNOLOGY
DEPARTMENT OF BIOMECHANICAL ENGINEERING

EXAMINATION COMMITTEE
prof. dr. S. Misra
dr. I.S.M. Khalil
prof. dr. ir. L. Abelmann

DOCUMENT NUMBER
BE - 837

UNIVERSITY OF TWENTE.

01-06-2023

Preface

Before you lies my thesis, named ”Scaling Rules for Microrobots with Full Energetic Autonomy”. This serves as the conclusion of my graduation assignment, part of the master's program of Biomedical Engineering at the University of Twente.

Over the course of this assignment, the goals have changed multiple times. It started off with modelling a self-regulating type of fuel cell but quickly turned to a more general aim of understanding the dynamics of a fuel cell. And the equations of motion, which later on became an important part of this thesis, started off as a mere thought experiment sketched on a piece of paper. Even though the final version of this thesis is far from what I expected at the start, I am very glad with the changes it underwent.

Prior to the writing of this thesis, part of this study has been presented at the International Conference on Manipulation, Automation and Robotics at Small Scales in 2022. It was an incredible experience to work together with a group of people from various backgrounds to achieve this and to be able to contribute to the scientific community.

I would like to thank my daily supervisor Islam Khalil for always being there to help me, both with technical and process-related questions and issues. I am also grateful to Leon Abelmann for the experience he shared and the critical thinking to keep the study relevant.

I would also like to thank my friends and family for their support, with special thanks to my girlfriend Geanne Welbergen.

Kind regards,

Erwin van Renselaar

Abstract

In the last decades, within the branch of medical care, minimally invasive surgery has received much attention. A promising example of this is the usage of untethered devices for diagnostic purposes as an alternative to colonoscopy. These devices, however, are currently powered by internal batteries which ensure a limited lifetime. Secondly, they are purely passive, moving with the peristaltic movement of the intestinal system. Other useful functionalities, such as performing biopsies and targeted drug delivery, are as of now impossible. Therefore untethered devices with full energetic autonomy are desired, that can generate electricity on board and possess a mechanism for locomotion. The aim of this study was to create a mathematical model of the end-to-end mechanics of such a capsule across different scales. A proton exchange membrane fuel cell is chosen as the power supply.

The first step in this process was to model the polarization plot of a fuel cell, based on experimental data. The constructed model is based on electrochemical laws, making the parameters used in the equation physically meaningful. Therefore the relationship between the size of the fuel cell and its polarization plot can be established. The current at which maximum power is generated as a function of size is subsequently used as input for the equations of motion.

The capsule is designed as a spherical head with a helical tail. The fuel cell is located in the head, together with a compartment where the fuel is stored. The chosen type of fuel is CaH_2, which reacts with water in the surrounding bodily fluids to form H_2, with which electricity can be generated. The current flows through a set of tri-axial coils, that can generate a magnetic torque under the influence of an external magnetic field. The helical tail then generates a translational velocity. This was modelled across scales, where the radius of the capsule decreases from $15\,\mathrm{mm}$ to $1.64\,\mathrm{mm}$. Over this range, the velocity is almost constant, decreasing from $5.4\,\mathrm{mm\,s^{-1}}$ to $5.3\,\mathrm{mm\,s^{-1}}$. The consumption rate for CaH_2 decreases quadratically, from $3.0 \times 10^{-2}\,\mathrm{mm^3\,s^{-1}}$ to $4.1 \times 10^{-4}\,\mathrm{mm^3\,s^{-1}}$. The lifetime of the capsule decreases linearly, from $58\,\mathrm{h}$ to $6.3\,\mathrm{h}$.

Using this mathematical model, the trends found for the translational velocity and the fuel consumption are favourable in scaling down, while that for the lifetime is not. In future research, experimental validation for these theoretical results is desired.

Contents

Abbreviations and symbols

List of abbreviations

CVS	cardiovascular system
GDL	gas diffusion layer
GIT	gastrointestinal tract
MEA	membrane electrode assembly
MFC	micro fuel cell
MFG	micro fuel generator
PEMFC	proton exchange membrane fuel cell
SRL	Surgical Robotics Lab
STP	standard temperature and pressure
UD	untethered device
UT	University of Twente

List of mathematical symbols

A	area of the fuel cell [m^2]
$a_{\mathrm{H_2}}$	chemical activity of H_2
$a_{\mathrm{H_2O}}$	chemical activity of H_2O
$a_{\mathrm{O_2}}$	chemical activity of O_2
$\boldsymbol{B}$	external magnetic field [T] $\in \mathbb{R}^3$
bl	bodylength [m]
c	experimental parameter [$\mathsf{V\,K^{-1}}$]
C_{C}	consumption rate of CaH_2 [$\mathsf{mm^3\,s^{-1}}$]
$C_{\mathrm{H_2O}}$	consumption rate of H_2O [$\mathsf{mm^3\,s^{-1}}$]
$C_{\mathrm{O_2}}$	consumption rate of O_2 [$\mathsf{mm^3\,s^{-1}}$]
e	elementary charge [$1.602 \times 10^{-19}\,\mathsf{C}$]
E^0	ideal cell potential [V]
E^0_{A}	potential at the anode [V]
E^0_{C}	potential at the cathode [V]
E_{FC}	output potential of the fuel cell [V]
E_{N}	adjusted Nernst potential in equilibrium [V]
I	current [A]
I_0	exchange current [A]
$\mathbf{I}_{\mathrm{eff}}$	vector of effective currents [A] $\in \mathbb{R}^3$
$\mathbf{I}_{\mathrm{in}}$	vector of the individual currents [A] $\in \mathbb{R}^3$
I_{L}	limiting current [A]
I_{tot}	current at maximum power [A]

l_c	length of the coil [m]
l_w	length of the wire [m]
$\boldsymbol{m}$	magnetic dipole moment [A m^2] $\in \mathbb{R}^3$
m_C	molar mass of CaH_2 [$42.094\,\mathrm{g\,mol^{-1}}$]
$m_{\mathrm{H_2O}}$	molar mass of H_2O [$18.02\,\mathrm{g\,mol^{-1}}$]
k	Boltzmann constant [$1.381 \times 10^{-23}\,\mathrm{J\,mol^{-1}\,K^{-1}}$]
N	number of windings of the coil
n	number of electrons transferred in one complete reaction
n_A	number of electrons transferred in the anodic reaction
n_C	number of electrons transferred in the cathodic reaction
P_d	power density [W m^{-3}]
P_E	electrical power [W]
P_R	rotational power [W]
P_T	translational power [W]
r_b	radius of the capsule and the fuel cell [m]
$r_{\mathrm{b,min}}$	smallest radius of the fuel cell [m]
r_c	radius of the coil [m]
Re	Reynolds number
R_O	ohmic resistance [Ω]
r_t	radius of the helical tail [m]
r_w	radius of the wire [m]
$r_{\mathrm{w,min}}$	smallest radius of the wire [m]
R_w	resistance of the wire [Ω]
S	surface area of the coil [m^2]
T_F	roomtemperature [K]
t_l	lifetime [s]
v	translational velocity [m s^{-1}]
V_act	activation overpotential [V]
V_con	concentration overpotential [V]
$V_{\mathrm{H_2}}$	crossover overpotential [V]
$V_{\mathrm{O_2}}$	molar volume of O_2 [$22.7 \times 10^3\,\mathrm{cm^3\,mol^{-1}}$]
V_OC	open-circuit voltage [V]
V_ohm	ohmic overpotential [V]
v_rel	relative velocity [s^{-1}]
α	charge transfer coefficient
β	scaling factor
η	viscosity [Pa s]
η_R	efficiency from electrical to rotational power [%]
η_T	efficiency from electrical to translational power [%]
θ	angle of the helical tail [rad]
ρ	density [kg m^{-3}]
ρ_C	density of CaH_2 [$1.7 \times 10^3\,\mathrm{g\,mm^{-3}}$]

$\rho_{\mathrm{H_2O}}$	density of H_2O $[997 \times 10^{-6}\,\mathsf{g\,mm^{-3}}]$
ρ_{w}	resistivity of the wire $[\Omega\,\mathsf{m}]$
$\boldsymbol{\tau}_{\mathrm{d}}$	drag torque $[\mathsf{N\,m}] \in \mathbb{R}^3$
$\boldsymbol{\tau}_{\mathrm{m}}$	magnetic torque $[\mathsf{N\,m}] \in \mathbb{R}^3$
$\boldsymbol{\phi}$	vector of angles of the dipole moments with respect to B $[\mathsf{rad}] \in \mathbb{R}^3$
$\dot{\boldsymbol{\phi}}$	time derivative of $\boldsymbol{\phi}$ $[\mathsf{rad\,s^{-1}}]$ $\in \mathbb{R}^3$
$\boldsymbol{\omega}$	vector of angular velocities $[\mathsf{rad\,s^{-1}}] \in \mathbb{R}^3$

List of Figures

List of Tables

Chapter 1

Introduction

Since Purcell's 1976 lecture on "*Life at low Reynolds number*" [1], and particularly in the last two decades, steady progress in imaging and microfabrication instrumentation has allowed us to create robotic systems at the micro scale [2], [3]. Feynman believed that machines could eventually be built on the scale of a human cell [4] and nature has inspired us to realize these machines in terms of locomotion methods, processes, materials, and designs. Nature's designs can be observed and theoretically understood in living systems, and this provides an approach for developing such robots and untethered device (UD).

1.1 Motivation

One of the many branches with a transition towards smaller instruments is that of medical care, more precisely in minimally invasive surgery [5]. Passive UDs, in the form of wireless capsules with an integrated camera, are already being used in clinical care as an alternative to colonoscopy. Its advantages are less discomfort for the patient and the ability to inspect a larger part of the gastrointestinal tract (GIT), as it moves along with the peristaltic movement of the patient. [6]

It is important to note, however, that this locomotion is purely passive, the UD is completely dependent on the motion of the bowel. If, for example, the camera is not orientated towards the desired part of the GIT at the right time, the clinician is unable to influence this and the UD passes by without the needed diagnostic information. Would active locomotion be possible, a multitude of other useful functionalities could be incorporated as well, e.g. performing biopsies and targeted drug delivery over the entire length of the GIT. [7] This would greatly benefit the diagnosis and treatment of diseases such as intestinal carcinoma.

Another potential medical application of UDs is found in the cardiovascular system (CVS). Due to the large differences in vascular diameters and blood flow, each segment of the CVS requires a different size of UD, ranging from a centimetre to a micrometre scale. Since environmental conditions in the CVS are more difficult than in the GIT, advances in this field have been slower. [8]

In scaling down these devices, two problems occur. The most obvious is the downsizing of the components that perform the desired functionalities. Considering the endoscopic pill, the locomotion, imaging, and delivery system should be designed to work on

the desired scale.

The second and less obvious problem relates to the resource needed for these actions: all these tasks need an energy supply. While scaling down, the energy density in the batteries becomes a limiting factor. [9] Combining more advanced functionalities inside the capsule, will only increase the power demand, and thus decrease its lifetime. This power shortage requires further research and thus will be part of the focus of this study. A solution to this problem is to find an alternative energy source, more suitable to scaling down.

Besides the energy supply, another issue is found in the end-to-end modelling of such a system. This technology is not yet advanced enough to translate microrobots into real-world applications. In contrast, we have known that living systems can transduce and connect chemical, electrical, and mechanical energy. However, a system capable of mimicking this biological pathway from start to finish has not yet been explored.

1.2 Energy Sources

Since the end goal is a useful product in a clinical, *in vivo*, setting not all energy sources are considered. Instead, this study focuses on the following four types: electromagnetism, electromagnetic radiation, acoustics and chemical energy. [10] These are one by one discussed in Subsections 1.2.1-1.2.4. In Subsection 1.2.5 the energy source most suitable to this purpose will be chosen.

1.2.1 Electromagnetism

Magnetism as an external stimulus has often been studied, and successfully, in combination with microbots. For instance, *Martel, et al.* [11] used magnetotactic bacteria inside an external magnetic field. This allowed them to gain full motion control, at velocities up to 150 times the length of the bacteria per second.

Another use for magnetic energy transduction was studied by *Li, et all.* [12], who looked at the inductive coupling between coils. They let current flow through two of them, and the other two were set up to convert the magnetic energy of the current into an induced current. This way they planned to charge in vivo sensors without transcutaneous wiring. Over a distance of 3 cm, they managed a 24% efficient power transfer. One important note however, this was planned to charge an implanted medical sensor, thus to use this for a moving device such as an endoscopic pill would require large design adjustments.

1.2.2 Electromagnetic radiation

The use of electromagnetic radiation as an external stimulus is often more limited due to the inability of some types of radiation to pass through thicker layers of skin, while other types of radiation come with health hazards.

In a study by *Steager, et al.* [13], the motion of a layer of bacteria was influenced by ultraviolet stimulation. The motion was self-coordinated by the bacteria, mostly based on chemotaxis. With the ultraviolet stimulation, they were able to stop the bacteria from mov-

ing, and after exposure, they continued with their self-coordinated motion.

In 2016, *Lozano, et al.* [14] managed to get directional in artificial microscopic spherical bodies. They made one hemisphere black, which under the stimulus of light, heats up more than the other side. This increased temperature in turn gives a difference in chemical concentrations between the two sides, which adjusts the self-coordination of the bacteria. Since bacteria by themselves move from a high-energy state to a lower one, the light had an intensity gradient in the direction of the desired motion.

1.2.3 Acoustics

Jin, et al. [15] have done a recent study on the use of acoustics as an external energy source. Similar to what *Li, et al.* studied the focus was on generating electricity in an implantable medical device. Instead of a set of coils, they used an ultrasound transducer and piezoelectric sensors. However, the efficiency of the magnetic system over 3 cm tissue, is equal to that of the acoustic system over just 5 mm tissue.

1.2.4 Chemical

The fourth external source, mentioned here, that can be used for energy transduction, is the group of chemical energy sources. The most widely spread variant of this is the combustion engine, where heat energy is generated by the combustion of a fuel. Since the energy is in the form of heat, which is less practical, and the generation of unwanted gases as byproducts, this is not seen as a valid idea for in vivo power generation.

Another well-known chemical energy source is the fuel cell, which is quite similar to a battery in the sense that it produces electricity with redox reactions. Various types of fuel cells exist, but due to the intended medical use, only low-temperature fuel cells are considered. The types that function below 100° are the proton exchange membrane fuel cell (PEMFC), the alkaline fuel cell and the direct methanol fuel cell. For *in vivo* use, having water as the only end product is highly favourable. Therefore the direct methanol fuel cell, with CO_2 as restproduct, is discarded as a viable option. [16] For the desired endgoal, the fuel cell needs to be sufficiently small. Since alkaline fuel cells are not as easily miniaturized as PEMFCs, the latter is chosen as the most viable option. [17]

As of now, PEMFCs are heavily studied and understood well, mostly because they show promise as suppliers of green energy. Therefore, most research is done on large systems, where for example fans for gas flow can be implemented. To use a PEMFC on e.g. an ingestible pill, it can be, at most, on a centimetre scale.

Integrated micro fuel cell with micro fuel generator

In the scope of this study, only miniaturization of a PEMFC does not suffice, the system for fuel supply, in this case hydrogen, has to be on that scale too. Therefore in this part, micro fuel cell (MFC)s with integrated micro fuel generator (MFG)s will be discussed.

A system with on-board hydrogen generation from water and metal hydrides has been shown by *Swaminathan, et al.* [18] to be smaller than 0.5 cm in all three dimen-

sions, which would be sufficiently small for on a chip. The hydrogen generation is self-regulated since its partial pressure has an effect on the water inlet to the hydride storage. A disadvantage of this channel system, however, is the limiting effect of mass transport of water before the diffusion of hydrogen gas would have been limiting. Also, the transport of water through an increasing amount of byproduct from hydrogen generation makes the system act less efficiently over time.

A system that was able to deliver higher currents, designed by *Kim* [19] used a hybrid power system. A PEMFC used a steady supply of hydrogen generated from sodium borohydride, to generate a steady current. This was connected to an auxiliary battery. Depending on the value of the load, the PEMFC would either charge the battery or the battery would assist the PEMFC during peak loads when the PEMFC alone could not deliver the required power. This way, the system had a larger buffer for high currents, but there was no control of the buffer. If a load would have been absent for long enough, theoretically the battery could saturate, leading to an uncontrolled increase in hydrogen pressure. Also, this system was 4 cm x 4 cm, thus a dramatic decrease in size is needed before it can be used in vivo.

A study by *Balakrishnan, et al.* [20] has been done on a micro fuel cell in which hydrogen is produced from again sodium borohydride. Here, however, the bubbles of hydrogen are transferred to small containers for storage, while they prevent the hydride to come into contact with the catalyst if hydrogen is built up beyond a certain level. Again, the hydrogen is oxidized by a PEMFC to generate electricity. Due to the build-up of hydrogen in both the containers and the catalytic reservoir, there is a supply, which can be refilled through the hydrolysis of the hydride. Although this sounds promising, this was merely a proof of concept, and there has been no follow-up as of now. Besides, without proper scales, the device seems to be larger than 3 cm in diameter, without the casing. Therefore, its size has to be decreased drastically. Also, this principle depends on the gas bubbles to float up in the fluid. However, in the human body, the capsule will rotate. When that happens, the hydrogen bubbles will not occupy the volume needed for hydrogen generation. Therefore, self-regulation will most likely not have the intended effect.

1.2.5 Chosen energy source

With electromagnetic radiation, only direct locomotion has been achieved. Since no electricity has been generated, other desirable functions, such as a camera would not be possible. For that reason, radiation will not be used in this study. Although electromagnetism and acoustics do generate electricity, they both have been used only with an implanted, and thus static, device. Introducing these energy sources on a moving object gives rise to difficulties in positioning the external device powering the object. Since in this study a movable UD is desired, these two energy sources will be discarded as well. The chosen energy source for this study then is a PEMFC with on-board hydrogen generation. In Section 1.3, this type of fuel cell will be further explained.

1.3 PEMFC

The proton exchange membrane fuel cell needs two fuels, hydrogen and oxygen, to generate electricity with water as the final product. Near room temperature, this reaction is spontaneous and exothermic, meaning energy is released. In Equations 1.1 and 1.2 respectively the anodic and cathodic half-reactions of this redox reaction between hydrogen and oxygen gas are given. [23]

$$2H_2 \longrightarrow 4H^+ + 4e^- \quad (1.1)$$

$$O_2 + 4e^- + 4H^+ \longrightarrow 2H_2O \quad (1.2)$$

As can be seen, electrons are released at the anode with the oxidation of H_2 and captured at the cathode with the reduction of O_2. If a load is present in the trajectory of the electrons, this can be powered by the electrical current supplied by the PEMFC.

In Figure 1.1(A) the general structure of a PEMFC can be seen. It is symmetrical in its layers, with the anode connected to the hydrogen storage, while the cathode is connected to the oxygen storage.

In the middle, the proton exchange membrane itself can be seen, which allows only the hydrogen ions to move to the cathode. On both sides it is connected to a catalyst, assisting in splitting hydrogen molecules on the anode and forming water from the oxidized hydrogen and reduced oxygen. Often platinum is chosen for this purpose because its Fermi level is lower than that of hydrogen but higher than that of H^+. This way the energy level is decreased in two smaller steps, leading to an overall lower activation energy. This, however, immediately leads to a disadvantage of the PEMFC, its high price.

The GDL ensures the proper distribution of the gases on the catalyst layer for increased efficiency. Due to its conductivity, it also allows the electrons to leave the catalyst. Often the catalyst is produced as a layer on the GDL, to form a gas diffusion electrode. The gasket then closes off the GDL so no gas can escape, and at the same time acts as an insulator.

The flow plates ensure the gas supply to the fuel cell, while staying in contact with both the current collector and the GDL. Subsequently, the current collectors function as the electrical connection between the fuel cell and the load. Finally, the end plates are insulating, and provide mechanical support to the PEMFC.

The membrane together with the catalysts, and sometimes the GDLs as well, is often called the MEA. [22] [23]

In Figure 1.1(B) the flow diagram of a PEMFC can be seen. At the anodic catalyst, the half-reaction found in Equation 1.1 occurs. Subsequently, the electrons move through the GDL, flow plates and current collector through the load to the cathode, to facilitate the reaction found in Equation 1.2. [22] [23]

1.4 Framework

This study has been done at the Surgical Robotics Lab Surgical Robotics Lab (SRL) of the University of Twente (UT). The experiments have been performed in the accompanying laboratory. There has been help from multiple organizations, particularly for further steps in this project. The research group Mesoscale Chemical Systems at the UT has

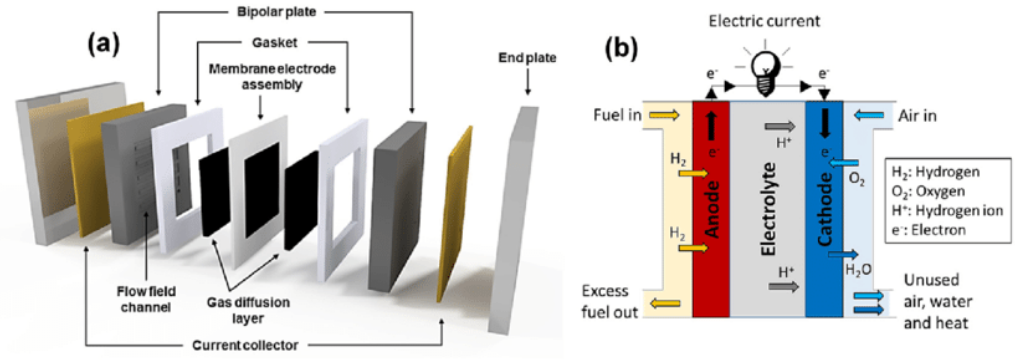

Figure 1.1: Here two different schematic overviews of a PEMFC can be seen. (A) The different layers that make up a PEMFC can be seen. The MEA is found in the middle, consisting of the proton exchange membrane and a catalyst on either side. On both sides of the MEA a GDL is seen, enclosed by a gasket. The bipolar plates, current collectors and endplates together form the exterior. (B) In the functional drawing, the hydrogen enters the fuel cell at the anode. On the catalyst it is split into hydrogen ions, that pass through the membrane, and electrons, that pass through the load. On the cathodic catalyst they form, together with oxygen, water as product. [21] [22]

helped in understanding the process of hydrogen generation. The Institute for Analytical and Bioanalytical Chemistry of Ulm University and Hahn-Schickard have contributed to this project by working on compartments for hydrogen generation for the proposed capsule.

This research was a novel addition to the department, with at the start no related projects. However, there will be multiple follow-up studies. One will focus on an end-to-end experiment in a static setting to validate the model proposed in this study, while another aims at designing an endoscopic capsule similar to the one proposed here.

1.5 Research question

This study aims to create a mathematical model of a UD with full energetic autonomy. This has to be an end-to-end model that encaptures the working mechanisms of the entire UD, from the generation of electricity to the mechanics of the capsule that lead to propulsion. The maximal propulsion velocity is chosen as the main result, as this is a highly quantifiable outcome. The second result is the fuel consumption needed to reach the maximal velocity. To understand the properties of such a capsule in various medical uses across scaling, the size of the UD is chosen as the main variable. [24]

This leads to the following research question:

How are swimming velocity and fuel consumption of an untethered device with full energetic autonomy affected when scaling down?

1.6 Report organization

In Chapter 2 a model of a fuel cell is constructed and experimentally tested. In Chapter 3 a model that incorporates the chemical,

electrical and mechanical properties of a capsule powered by said fuel cell is constructed and simulated. In Chapter 4 an extrapolation is performed on the results of the previous chapter, alongside a listing of shortcomings in this study. Finally, in Chapter 5 the conclusions to the research question are presented, and recommendations for future studies are given.

Chapter 2

Polarization Curve

Since this study aims at understanding the scaling rules of microbots powered by fuel cells, first a mathematical model of a fuel cell is needed. In Section 2.1 the concept of a polarization plot will be explained, which is an important characterization of a fuel cell. In Section 2.2 a mathematical model, based on a set of parameters, for such a plot will be derived. Subsequently, in Section 2.3 experiments are discussed to find these parameters. Finally, in Section 2.4, this will be connected to Chapter 3.

2.1 Introduction

As discussed in Section 1.3, a PEMFC plays a vital part in the transduction of chemical energy to electrical energy. Similar to all other known processes, PEMFCs are exposed to losses in energy. This can be thought of as follows. The end product of a PEMFC is DC electricity, which is characterized by two variables. The first one is the generated current (I), which is directly correlated to the number of H_2 and O_2 molecules that react per second, as seen in Equations 2.1 and 2.2.

$$2H_2 \longrightarrow 4H^+ + 4e^- \tag{2.1}$$

$$O_2 + 4e^- + 4H^+ \longrightarrow 2H_2O \tag{2.2}$$

The second variable is the output potential of the fuel cell (E_{FC}), which corresponds to the amount of energy in these electrons. The energy losses mentioned earlier, are represented most clearly in deviations in the E_{FC} from the ideal value. In short, a polarization plot shows the relationship between the I and E_{FC}.

The ideal E_{FC} can be thought of as follows. Since a fuel cell is based on redox reactions, the voltages in the PEMFC can be represented by the potential at the anode (E^0_{A}) and the potential at the cathode (E^0_{C}). In this case, E^0_{A} is the potential of the half-reaction seen in Equation 1.1, which is defined as the reference to which all other standard potentials are measured, thus E^0_{A} is $0\,\mathsf{V}$. The E^0_{C} equals $1.22\,\mathsf{V}$. [25] Therefore, the ideal cell potential (E^0) is given in Equation 2.3.

$$E^0 = E^0_{\mathrm{C}} - E^0_{\mathrm{A}} = 1.22\,\mathsf{V} \tag{2.3}$$

In Figure 2.1 an example of a polarization plot can be seen. The black dashed line labelled as ideal voltage equals E^0. The grey line shows the actual polarization plot, i.e. the I-E_{FC} dependency. In this figure, four deviations from the E^0 can be seen.

The first loss discussed is the activation overpotential (V_{act}), which occurs due to the activation barrier that must be overcome in

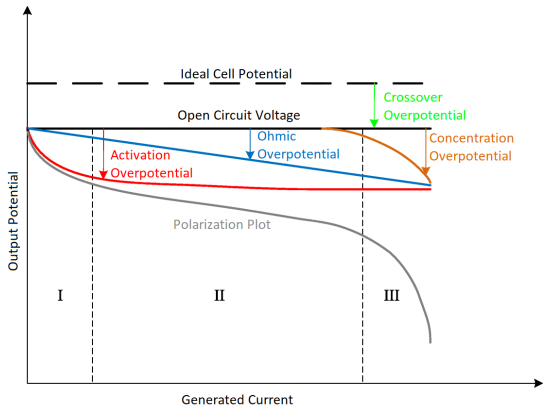

Figure 2.1: Example of a polarization plot [26]. On the y-axis the output voltage of the fuel cell is shown, while the x-axis represents the current generated by the half-reactions. In the grey line the polarization plot can be seen. The deviation of this curve from the ideal cell potential is divided into four overpotentials. In red the activation overpotential can be seen, which is most prominent at low currents. The ohmic overpotential is shown in blue, this gives the linear region in the middle. The concentration overpotential is shown in orange, and it occurs mostly near the limiting current. The fourth and final deviation is the crossover overpotential, which is seen in green. This is the main difference between the ideal cell potential and the potential measured in open circuit.

any reaction. Multiple reactions occur at the anodic platinum catalyst layers as seen in Equations 2.4 and 2.5. [27]

$$\mathrm{H_2} + 2\,\mathrm{Pt} \longrightarrow 2\,\mathrm{PtH} \tag{2.4}$$

$$2\,\mathrm{PtH} \longrightarrow 2\,\mathrm{Pt} + 2\,\mathrm{H^+} + 2\,\mathrm{e^-} \tag{2.5}$$

Similarly, the reactions seen in Equations 2.6 and 2.7 occur at the cathode. [28] [29]

$$\mathrm{O_2} + 2\,\mathrm{Pt} \longrightarrow 2\,\mathrm{PtO} \tag{2.6}$$

$$2\,\mathrm{PtO} + 4\,\mathrm{H^+} + 4\,\mathrm{e^-} \longrightarrow 2\,\mathrm{Pt} + 2\,\mathrm{H_2O} \tag{2.7}$$

Although platinum is one of the most energetically favourable catalysts [30], all reactions still need to overcome the bond energies in these reactions. Since this energy is lost in the process, the amount of energy in this current has decreased, which can be seen as a potential drop in the output voltage. [31]

The second voltage loss, ohmic overpotential (V_{ohm}), is caused by the ohmic resistance (R_{O}). In most electrical systems, only the negative charges are transferred. However, since the H^+-ions move through the electrolyte in a PEMFC, R_{O} also incorporates the resistance these cations encounter. [32]

The third voltage loss, the concentration overpotential (V_{con}), comes from the depletion of the reactants H_2 and O_2 near the membrane. Although the partial pressures of these gases in the bulk remain unchanged, a pressure gradient occurs near the membrane, since their mass transfer is physically limited. This means at currents near the limiting current (I_{L}) a local decrease in partial pressure and thus voltage arises. [33]

The final loss that will be discussed is the difference between E^0 and the open-circuit voltage (V_{OC}). This occurs due to imperfections in the PEMFC, specifically the crossover of H^+ in open-circuit. The result is called the crossover overpotential ($V_{\mathrm{H_2}}$). [34]

2.2 Modelling

As mentioned in Section 2.1, multiple potential losses occur in a fuel cell. In order to model a fuel cell correctly, these voltage losses will be expressed individually in mathematical form.

Regarding the V_{act}, in working with activation energies, the Butler-Volmer equation can be used, as seen in Equation 2.8,

$$I = I_0 \times \left(e^{\frac{\alpha n_\mathrm{A} e V_\mathrm{act}}{k T_\mathrm{F}}} - e^{\frac{-(1-\alpha) n_\mathrm{A} e V_\mathrm{act}}{K T_\mathrm{F}}} \right), \tag{2.8}$$

with the exchange current (I_0), the number of electrons transferred in the anodic reaction (n_A) (i.e., n_A= 2), the elementary charge (e), the Boltzmann constant (k), the roomtemperature (T_F) and the charge transfer coefficient (α)$\in$ $[0, 1]$. When α is unknown, it is often chosen to be 1/2. This gives Equation 2.9, which can be rewritten as Equation 2.10.

$$I = 2 I_0 \sinh\left(\frac{n_\mathrm{A} e V_\mathrm{act}}{2 k T_\mathrm{F}} \right) \tag{2.9}$$

$$V_\mathrm{act} = \frac{2 k T_\mathrm{F}}{n_\mathrm{A} e} \operatorname{arsinh}\left(\frac{I}{2 I_0} \right) \tag{2.10}$$

Equation 2.10 can be used to calculate the activation overpotential. [35] [36]

The V_act can be expressed using Ohm's law, which states that the voltage drop over the fuel cell is equal to Equation 2.11. [36], [37]

$$V_\mathrm{ohm} = R_\mathrm{O} I \tag{2.11}$$

The effect of the V_con, which has to be considered for both the anode and the cathode, is shown in Equation 2.12, [36]

$$V_\mathrm{con} = \left(1 + \frac{1}{\alpha}\right) \left(\frac{k}{n_\mathrm{A} e} + \frac{k}{n_\mathrm{C} e} \right) \times T_\mathrm{F} \ln\left(\frac{I_\mathrm{L}}{I_\mathrm{L} - I} \right), \tag{2.12}$$

with the number of electrons transferred in the cathodic reaction (n_C). The I_L is defined as the lowest current no longer attainable by the PEMFC, which is an implication of Equation 2.12.

From the literature, it is known, however, that the first part is not always in line with experimental values. Therefore V_con is redefined anew in Equation 2.13,

$$V_\mathrm{con} = c T_\mathrm{F} \ln\left(\frac{I_\mathrm{L}}{I_\mathrm{L} - I} \right), \tag{2.13}$$

with the experimental parameter (c) a constant that should be found empirically. [36], [37]

The fourth and final voltage loss is the V_{H_2}. Similar to the study done by *Li et al.* (2022), V_{H_2} is treated as a constant voltage loss [34]. Therefore it can be seen as the difference between the E^0 and the V_OC. Since E^0 is valid at standard temperature and pressure (STP), a correction for temperature and pressure is used as seen in Equation 2.14,

$$E_\mathrm{N} = E_\mathrm{e}^0 + \frac{k T_\mathrm{F}}{n e} \ln\left(\frac{\left(a_{\mathrm{H}_2}\right)^2 a_{\mathrm{O}_2}}{\left(a_{\mathrm{H_2O}}\right)^2} \right), \tag{2.14}$$

with the adjusted Nernst potential in equilibrium (E_N) and the number of electrons transferred in one complete reaction (n) (i.e., n = 4). [38] Furthermore, the chemical activity of H_2 (a_{H_2}) and the chemical activity of O_2 (a_{O_2}) are needed. The assumption is made that, in the range of pressures relevant to this experiment, i.e. close to atmospheric pressure, these gases are close to ideal. In that case, activity approximately equals the ratio between the effective partial pressure and partial pressure under STP. [39] Finally, as water is produced as a liquid, the chemical activity of $\mathrm{H_2O}$ ($a_{\mathrm{H_2O}}$) equals one. It is important to note that the E_N only applies to systems in equilibrium, i.e. in the absence of a net current.

Combining the information stated above, V_{H_2} is the difference between E_N and V_OC as seen in Equation 2.15.

$$V_{\mathrm{H}_2} = E_\mathrm{N} - V_\mathrm{OC} \tag{2.15}$$

Thus, the E_{FC} can be expressed symbolically as in Equation 2.16 and mathematically as seen in Equation 2.17 [24].

For Equation 2.17 to have practical implications in modelling this PEMFC, the parameters $V_{\mathrm{H_2}}$, I_0, R_{O}, c and I_{L} have to be found experimentally.

2.3 Experiments

With this in mind, experiments need to be performed to find the values of these five parameters.

The fuel cell used to perform these experiments, was the SOLAR HYDROGEN SCIENCE KIT by HORIZON EDUCATIONAL. For the load, a VOLTCRAFT V-CHARGE 60 was used to control the current. Furthermore, a DC power supply was used to power the battery charger and two multimeters, one to measure the output voltage of the fuel cell and one to measure the input current.

Besides the parameters stated above, certain variables are needed as well. For these experiments $T_{\mathrm{F}} = 292.5\,\mathsf{K}$, and both $a_{\mathrm{H_2}}$ and $a_{\mathrm{O_2}}$ were calculated to be approximately 1.13 via the ideal gas law.

The V_{OC}, the potential at $I = 0\,\mathsf{A}$, was measured as $0.98\,\mathsf{V}$. Using Equation 2.15, $V_{\mathrm{H_2}}$ was calculated as $0.45\,\mathsf{V}$.

To find the other four parameters, FMINCON by MATLAB was used for estimation. The summarized algorithm is found in Algorithm 1.

Algorithm 1 Parameter identification

1: **Define** ranges for I_0, R_{O}, I_{L} and c
2: **Define** constants
3: **Define** measured input I and output E_{FC}
4: **Define** symbolic Equation 2.17
5: **Calculate** the optimal set of parameters by minimizing the error between the measured voltage and calculated voltage, using FMINCON

The measurements with standard deviations can be seen as red points in Figure 2.2(A) and the resulting fitted model as the black line in the same figure. The values of the five parameters used for the model can be found in the second column of Table 2.1. The model seems to be a very good estimation of the measurements, with a calculated MSE of $5.1 \times 10^{-5}\,\mathsf{V}^2$. Especially at higher currents, the values predicted by the model fall within one standard deviation of the measurements. At lower currents, the deviations are larger. A waveform is present, where near $0.2\,\mathsf{A}$ the measurements are higher than the predicted model, and near $0.4\,\mathsf{A}$ the opposite can be seen.

This could be caused by a fault in either the model or the measurements. Since this waveform does not correspond to polarization plots found in literature, the latter is assumed.

2.4 Connection to equations of motion

Using the set of parameters derived in Section 2.3, which can be seen in the middle column in Table 2.1, it is possible to calculate the electrical power (P_{E}) as a function of the I. This is shown in Figure 2.2(B). Similar to the polarization plot in Figure 2.2(A), the measurements near $0.2\,\mathsf{A}$ are slightly higher than the model, and vice versa near $0.4\,\mathsf{A}$.

$$E_{\mathrm{FC}} = E_{\mathrm{e}}^{0} - V_{\mathrm{H_2}} - V_{\mathrm{act}} - V_{\mathrm{ohm}} - V_{\mathrm{con}} \tag{2.16}$$

$$E_{\mathrm{FC}} = E_{\mathrm{e}}^{0} - V_{\mathrm{H_2}} - \frac{2kT_{\mathrm{F}}}{n_{\mathrm{A}}e}\,\mathrm{arsinh}\left(\frac{I}{2I_0}\right) - R_{\mathrm{O}}I - cT_{\mathrm{F}}\ln\left(\frac{I_{\mathrm{L}}}{I_{\mathrm{L}} - I}\right) \tag{2.17}$$

Since this waveform is present in the voltage curve, it can be seen in the power curve as well.

In Chapter 3, the peak in this P_{E} will be used as a starting point for the equations of motion. Since this peak will change across scales, it is important to understand the effect scaling has on the five parameters. Firstly, it is expected that R_{O} will increase linearly for a decreasing area of the fuel cell (A), similar to what other electrical components such as a wire show. The opposite is expected for I_0, which is a product of the A and the exchange current density, with the latter being a property of the combination of catalyst and half reaction. [35], [36] The same holds for the I_{L}, since it is expected that a given PEMFC has a maximum current density it can generate.

For the $V_{\mathrm{H_2}}$, both statements are relevant. The current produced by the fuel crossover is a product of a current density and its A, while the resistance through which this current flows is inversely proportional to the A [40]. Ohm's law then states that $V_{\mathrm{H_2}}$ remains equal across scaling.

$$c = \left(1 + \frac{1}{\alpha}\right)\left(\frac{k}{n_{\mathrm{A}}e} + \frac{k}{n_{\mathrm{C}}e}\right) \tag{2.18}$$

Finally, the parameter c, as it is derived from Equation 2.12, is given in Equation 2.18. Judging from this, c only depends on the types of half-reactions, and should thus stay constant across scaling. The relations of these five parameters to the area of the fuel cell are summarized in the right column of Table 2.1.

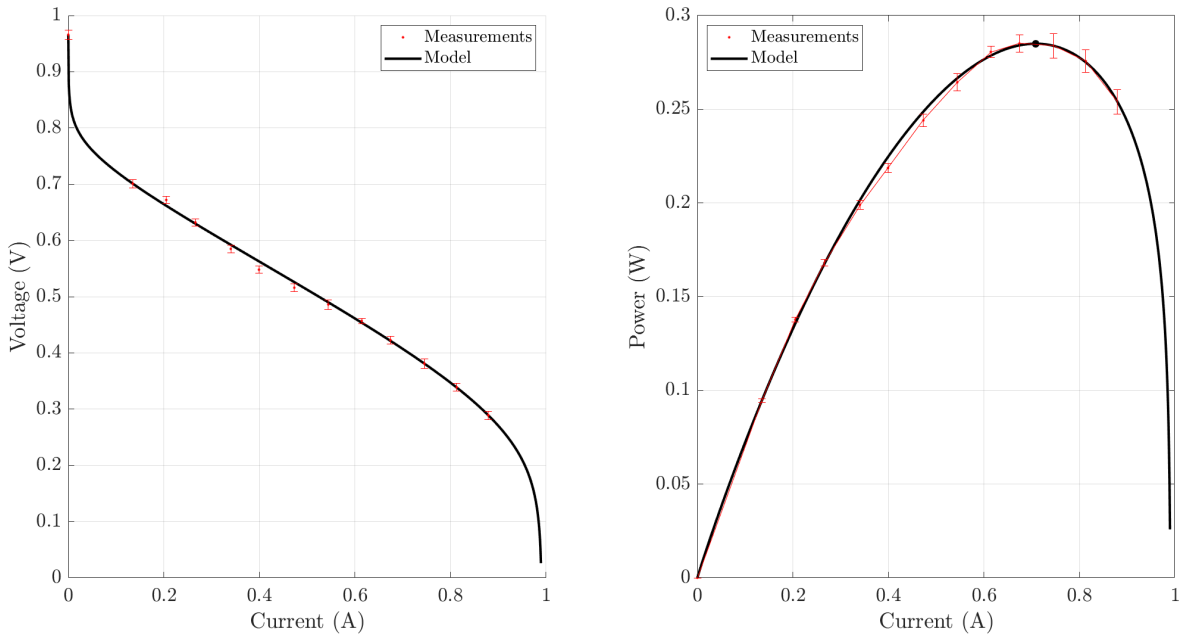

Figure 2.2: Experimental values of the fuel cell and the result of the fitting model. (A) Polarization (I-V curve) of the fuel cell. In red the average voltage measurements are shown for a range of currents. The corresponding standard deviations are shown in the red bars. In black the model of the polarization is presented, using Equation 2.17 with $I_0 = 3.19 \times 10^{-5}\,\mathsf{A}$, $R_\mathrm{O} = 0.33\,\Omega$, $c = 1.88 \times 10^{-4}\,\mathsf{V\,K^{-1}}$, $I_\mathrm{L} = 0.97\,\mathsf{A}$, and $V_{\mathrm{H}_2} = 0.26\,\mathsf{V}$. In general, the model seems to be a good approximation of the fuel cell, with an MSE of $5.1 \times 10^{-5}\,\mathsf{V}^2$. At high currents, the modelled value falls within the error bars, however at lower currents this is not always the case. (B) By multiplying the I and E_FC measurements, the red dots are calculated. The red error bars show the corresponding standard deviations, which are quite small compared to the power. The power calculated with the fitted model is seen in the black line. With the asterisk, the peak power is shown, which is needed in Chapter 3. Similar to the polarization plot in (A), at high currents the simulated power is within the error bars, while at lower current larger deviations are seen.

Table 2.1: The experimental parameters found in Section 2.3. In the left column the name of the parameter is given. The second column holds the values of these parameters as found using the optimization technique. The third column holds the standard deviations of this optimization. The fourth and final column hypothesizes the relation of the parameter with the active area of the fuel cell. This is needed in order to simulate the effects of downscaling of the fuel cell.

Parameter	Experimental value	Standard deviation	Relation to area A
I_0	$3.43 \times 10^{-5}\,\mathsf{A}$	$1.64 \times 10^{-6}\,\mathsf{A}$	$\propto$A
R_O	$0.35\,\Omega$	$3.32 \times 10^{-5}\,\Omega$	$\propto 1/\mathrm{A}$
c	$1.78 \times 10^{-4}\,\mathsf{V\,K^{-1}}$	$3.33 \times 10^{-6}\,\mathsf{V\,K^{-1}}$	Constant
I_L	$0.99\,\mathsf{A}$	$1.82 \times 10^{-4}\,\mathsf{A}$	$\propto$A
V_{H_2}	$0.26\,\mathsf{V}$	$8.4 \times 10^{-3}\,\mathsf{V}$	Constant

Chapter 3

Equations of motion

In Section 3.1 a design, based on Figure 3.1(A), is proposed. In Section 3.2 this design is modelled to calculate forward velocity and fuel consumption across scaling. In Section 3.3 the proposed model will be used for a specific design.

3.1 Introduction

A schematic design, similar to the UD used in this study, is shown in Figure 3.1(A). In Figure 3.1(B) a summary of the end-to-end process is stated. The upper hemisphere of the capsule is filled with CaH_2, which gives a hydrolysis reaction when combined with water from the surroundings. The hydrogen that is released in this reaction supplies the PEMFC with fuel, which allows for the generation of electricity. By letting this current flow through a set of tr-axial coils a vector of angular velocities ($\boldsymbol{\omega}$) is generated, which leads to a translational velocity (v) by helical propulsion. Two alterations were made to Figure 3.1(A) to show a clearer figure. These changes are that the model used in calculations has a spherical body and the helix is positioned as a tail. [24]

Since the aim is to study the effect of downscaling, radius of the capsule and the fuel cell (r_{b}) is chosen as the main variable. This in turn dictates the amount of fuel that needs to be consumed to generate the I at peak power. Letting that current flow through a set of tri-axial coils creates a magnetic dipole moment ($\boldsymbol{m}$), that can rotate the UD in an external magnetic field. If an adequate design for the UD is given, this rotation can be used to generate forward propulsion.

3.2 Construction of the model

In Subsections 3.2.1, 3.2.2 and 3.2.3 the electrical properties of the PEMFC, as found in Section 2.4, will be used to find equations for the rotational, and then the translational properties of the capsule. Afterwards, in Subsection 3.2.4 the equations for powers and efficiencies will be given, while in Subsection 3.2.5 equations for the fuel consumption rates will be given.

3.2.1 Electrical domain

The current that is drawn by the fuel cell depends on the size of the capsule and on the electrical load. Since this is about the maximum speed, the current at maximum power

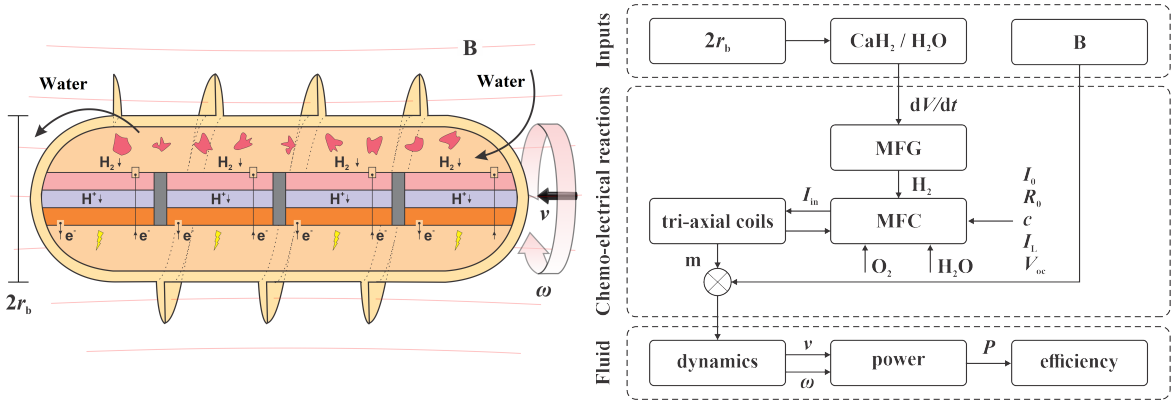

Figure 3.1: The end-to-end process predicts the angular and translational velocity, $\boldsymbol{\omega}$ and v, for a given body size $2r_\mathrm{b}$ of the untethered device (UD) and a $\boldsymbol{B}$. The r_b dictates the generated current, and thus the consumption rate of H_2 from CaH_2 in the micro fuel generator (MFG). The crossover potential V_{H_2}, the exchange current I_0, the internal resistance R_0, the parameter c and the limiting current I_L characterize the fuel cell (PEMFC). The interaction of $\boldsymbol{B}$ and I generates a magnetic torque τ_m, which rotates the UD at $\boldsymbol{\omega}$, and propels it at v. Finally the power P and efficiency are calculated. (A) Graphic overview of the capsule. (B) Functional overview of the dynamics occurring the capsule.

(I_tot) is considered. In this derivation a spherical body is assumed with the fuel cell on the middle plane.

To ensure this I_tot is passed on through the tri-axial coils, impedance matching between the PEMFC and the coils, is achieved as shown in Equation 3.1,

$$R_\mathrm{w} = \frac{E_\mathrm{FC}}{I_\mathrm{tot}} = \rho_\mathrm{w}\frac{l_\mathrm{w}}{\pi r_\mathrm{w}^2}, \tag{3.1}$$

with the resistance of the wire (R_w), the resistivity of the wire (ρ_w), the length of the wire (l_w) and the radius of the wire (r_w).

3.2.2 Rotational domain

For translating the UD using a static magnetic field, at least two requirements are needed. The first is a geometry that allows for drag-based propulsion upon rotation with respect to a desired axis rotation (i.e., the long axis of the helical body). The second requirement is to generate a dipole moment using the current drawn by the electromagnetic coils in a time-periodic manner. To calculate this, first the vector of the individual currents ($\mathbf{I}_\mathrm{in}$) is defined in Equation 3.2.

$$\sum |\mathbf{I}_\mathrm{in}| = I_\mathrm{tot} \tag{3.2}$$

This moment has to be rotated about a desired axis of rotation. In this case, magnetic torque ($\boldsymbol{\tau}_\mathrm{m}$) will balance drag torque ($\boldsymbol{\tau}_\mathrm{d}$), resulting in angular velocities and, because of the helical shape, the translational velocity.

Since the torque will cause the coils to rotate with respect to the external magnetic field, Lenz's law dictates that an induced current will occur that opposes the desired rotation. Therefore the vector of effective currents ($\mathbf{I}_\mathrm{eff}$) is defined as seen in Equation 3.3,

$$I_{\mathrm{eff},i} = I_{\mathrm{in},i} - \frac{2N\|\boldsymbol{B}\|S\sin(\phi_i)\dot{\phi}_i}{R_\mathrm{w}} \quad \text{for } i = 1,2,3, \tag{3.3}$$

with the number of windings of the coil (N), the surface area of the coil (S), the vector of

angles of the dipole moments with respect to B (ϕ) and the time derivative of ϕ ($\dot{\phi}$). The derivation of Equation 3.3 can be found in Appendix A.

A torque balance is set up with the $\boldsymbol{\tau}_{\mathrm{m}}$ and the $\boldsymbol{\tau}_{\mathrm{d}}$ [41] as seen in Equations 3.4 and 3.5.

$$\boldsymbol{\tau}_{\mathrm{m}} = \boldsymbol{\tau}_{\mathrm{d}} \tag{3.4}$$

$$NS\boldsymbol{I}_{\mathrm{eff}} \times \boldsymbol{B} = 8\pi\eta r_{\mathrm{b}}^{3}\boldsymbol{\omega} \tag{3.5}$$

Using Equation 3.5, $\boldsymbol{\omega}$ around the longitudinal axis can be calculated.

This relation holds for low-Reynolds number (Re), calculated in Equation 3.6,

$$Re = \frac{2r_{\mathrm{b}}\rho\|\boldsymbol{v}\|}{\eta} < 1, \tag{3.6}$$

for a fluid with density (ρ) and viscosity (η). If Re is larger than 1, inertial effects should be taken into account, making the purely drag-based model in Equation 3.5 no longer applicable.

3.2.3 Translational domain

To translate this rotation into a forward motion, a simplified model of a rigid helical body in low-Re is used in Equation 3.7 [42]. This holds for $\boldsymbol{\omega}$ about the longitudinal axis and v in the longitudinal direction,

$$v = \omega r_{\mathrm{t}} \left(\frac{\sin(2\theta)}{3 - \cos(2\theta)} \right), \tag{3.7}$$

with the radius of the helical tail (r_{t}) and the angle of the helical tail (θ).

With v it is also possible to calculate the relative velocity (v_{rel}) as seen in Equation 3.8, with bodylength (bl).

$$v_{\mathrm{rel}} = \frac{v}{bl} \tag{3.8}$$

3.2.4 Powers and efficiencies

To gain insight into how much energy is lost in the system, and specifically in which transition, efficiencies are particularly useful. Three different powers are distinguished, i.e. P_{E}, rotational power (P_{R}) and translational power (P_{T}) [41]. They can be found by multiplying the effort variable with the flow variable in each corresponding domain, as shown in Equations 3.9, 3.10 and 3.11.

$$P_{\mathrm{E}} = E_{\mathrm{MFC}} I \tag{3.9}$$

$$P_{\mathrm{R}} = \boldsymbol{\tau}_{\mathrm{m}}^{T}\boldsymbol{\omega} \tag{3.10}$$

$$P_{\mathrm{T}} = 6\pi\eta r_{\mathrm{b}} v^{2} \tag{3.11}$$

The efficiency from electrical to rotational power (η_{R}) and efficiency from electrical to translational power (η_{T}) can be found in Equations 3.12 and 3.13.

$$\eta_{\mathrm{R}} = \frac{P_{\mathrm{R}}}{P_{\mathrm{E}}} \times 100\% \tag{3.12}$$

$$\eta_{\mathrm{T}} = \frac{P_{\mathrm{T}}}{P_{\mathrm{E}}} \times 100\% \tag{3.13}$$

3.2.5 Fuel consumptions

The fuel cell needs both H_2 and O_2, with the former theoretically supplied by the hydrolysis of CaH_2. In this case, water is needed for hydrolysis, of which the reaction is seen in Equation 3.14.

$$\mathrm{CaH_2} + 2\mathrm{H_2O} \quad \longrightarrow \quad \mathrm{Ca(OH)_2} + 2\mathrm{H_2} \tag{3.14}$$

Combining Equation 3.14 with Equation 1.1, it is found that the molecular ratio of electrons to CaH_2 is 4 to 1, while that of electrons to H_2O is 2 to 1. Using Equation 1.2, it can be found that the molecular ratio of electrons to O_2 is 4 to 1. With

that in mind the consumption rate of CaH_2 (C_C), consumption rate of H_2O (C_{H_2O}) and consumption rate of O_2 (C_{O_2}) are found by using Equations 3.15, 3.16 and 3.17,

$$C_C = \frac{I_{tot}}{4F}\frac{m_C}{\rho_C}, \tag{3.15}$$

$$C_{H_2O} = \frac{I_{tot}}{2F}\frac{m_{H_2O}}{\rho_{H_2O}}, \tag{3.16}$$

$$C_{O_2} = \frac{I_{tot}}{4F}V_{O_2}, \tag{3.17}$$

with the molar mass of CaH_2 (m_C), the molar mass of H_2O (m_{H_2O}), the molar volume of O_2 (V_{O_2}), the density of CaH_2 (ρ_C) and the density of H_2O (ρ_{H_2O}).

3.3 Numerical values

Using Equations 3.1-3.17, it is possible to calculate the v and consumption rates for a specific design of a capsule similar to the one shown in Figure 3.1(A). The same subsections as in Section 3.2 are used.

3.3.1 Electrical domain

For this part, a design of the tri-axial coils will be presented. To calculate the desired dimensions of these coils, some mathematical constraints need to be derived.

Using the expected relations in Table 2.1, current at which the fuel cell generates maximum power can now be mathematically derived. To do so, the P_E is calculated by multiplying Equation 2.17 with I, and subsequently the derivative of P_E with respect I is taken, which gives Equation 3.18.

Using the relations in Table 2.1, the values for the five parameters can be calculated as a function of r_b. Setting Equation 3.18 equal to zero then gives a relation between the r_b and the I_{tot}. After that, the E_{FC} at that current and set of parameters can be calculated, so the left hand side of Equation 3.1 is known. Since the R_w is needed across scaling, an equation relating it to r_b is needed. A fitted equation was found in Equation 3.19, with an MSE of $9 \times 10^{-29}\,\Omega^2$.

$$R_w = 1.63 \times 10^{-4}\frac{1}{r_b^2} \tag{3.19}$$

Since this is qualitatively a good fit, r_w is chosen to have a linear relationship with r_b, with yet unknown scaling factor (β), i.e. $r_w = \beta r_b$. This design choice removes the dependence on size in Equation 3.1. Since a circular coil is assumed, with radius of the coil (r_c), $l_w = 2\pi N r_c$. These three assumptions, together with Equations 3.1 and 3.1, lead to Equation 3.20.

$$\text{Constraint 1:} \qquad 1.63 \times 10^{-4} = \rho_w \frac{2Nr_c}{\beta^2} \tag{3.20}$$

As for the wire, it is assumed to be made of copper, with $\rho_w = 0.33\,\Omega\,\mathrm{m}$. The smallest radius of the wire ($r_{w,min}$) is chosen to be an arbitrarily small value, i.e. $5\,\mu\mathrm{m}$. This gives the second constraint in Equation 3.21.

$$\text{Constraint 2:} \qquad r_{w,min} = \beta r_{b,min} \tag{3.21}$$

This calculation is implemented for rotation around one global axis, and thus a current through one resistance. However, the purpose of these calculations is to find the maximal v, that can always be achieved, therefore the worst scenario is assumed. Since the design includes tri-axial

$$\begin{aligned}\frac{\partial P_{\mathrm{E}}}{\partial I} =& E_{\mathrm{e}}^{0} - V_{\mathrm{H_2}} - \frac{2RT_{\mathrm{F}}}{e_{\mathrm{A}}F}\left(\operatorname{arsinh}\left(\frac{I}{2I_0}\right) + \frac{I}{\sqrt{I^2+I_0^2}}\right) \\ & - 2R_{\mathrm{O}}I - cT_{\mathrm{F}}\left(\frac{I}{I_{\mathrm{L}}-I} + \ln\left(\frac{I_{\mathrm{L}}}{I_{\mathrm{L}}-I}\right)\right)\end{aligned} \tag{3.18}$$

coils with parallel resistances, the total resistance equals $1/3$ of that. Therefore each coil is designed such that there is space for one that is three times as long. To fit the coil inside one hemisphere at smallest radius of the fuel cell ($r_{\mathrm{b,min}}$), r_{c} is chosen to be $\sqrt{2}/4$ $r_{\mathrm{b,min}}$ and length of the coil (l_{c}) to be $\sqrt{2}/3$ $r_{\mathrm{b,min}}$. However, l_{c} also equals $2Nr_{\mathrm{w,min}}$. Therefore the third and fourth constraints are seen as in Equations 3.22 and 3.23.

$$\text{Constraint 3:} \qquad r_{\mathrm{c}} = \frac{\sqrt{2}}{4} r_{\mathrm{b,min}} \tag{3.22}$$

$$\text{Constraint 4:} \qquad \frac{\sqrt{2}}{4} r_{\mathrm{b,min}} = 2Nr_{\mathrm{w,min}} \tag{3.23}$$

Now four mathematical constraints have been derived, and with four unknown positive parameters (N, r_{c}, β and $r_{\mathrm{b,min}}$) this can be solved uniquely. The total set of constraints together with solutions for the parameters are provided in Table 3.1.

The chosen range for r_{b} is set from $1.64\,\mathrm{mm}$ to $15\,\mathrm{mm}$. For this range, I_{tot} is shown as the black line in Figure 3.2A. In scaling down r_{b} from $15\,\mathrm{mm}$ to $1.64\,\mathrm{mm}$, I_{tot} is seen to have a quadratic decrease from $0.53\,\mathrm{A}$ to $6.3\,\mathrm{mA}$.

It is now possible to obtain results from the equations of motion. Besides these constraints, some other choices have been made during calculation. Again, since the goal is to calculate the highest velocity that can be constantly achieved, in Equation 3.3 all elements of $\boldsymbol{\phi}$ are set to $\pi/2$ rad to maximize the back emf.

3.3.2 Rotational domain

The first step in applying the method described in Subsection 3.2.2, is to define the global frame. The $\boldsymbol{B}$ is oriented such that it only has a positive x-component, thus $\boldsymbol{B} = [B, 0, 0]^T$.

The next design choice is that the capsule is oriented in the positive y-axis, i.e. ω_2 is the desired axis of rotation. The coil needed to generate this rotation is the one with dipole moment along the z-axis, i.e. $I_{\mathrm{eff},3}$. The back-EMF then occurs in the coil of which the dipole moment deviates from the magnetic field, i.e. $I_{\mathrm{eff},1}$. This reasoning, together with Equations 3.3 and 3.5, leads to Equation 3.24. In this case, $\dot{\phi}_1$ equals ω_2.

$$\begin{bmatrix} NBSI_{\mathrm{in},3} \\ I_{\mathrm{in},1}R_{\mathrm{w}} \\ I_{\mathrm{in},1} + I_{\mathrm{in},3} \end{bmatrix} = \begin{bmatrix} 8\pi\eta r_{\mathrm{b}}^3\omega_2 \\ 2NBS\sin(\phi_1)\omega_2 \\ I_{\mathrm{tot}} \end{bmatrix} \tag{3.24}$$

Using this method, the induced current $I_{\mathrm{eff},1}$ can be correctly negated. In this exact configuration the corresponding dipole is perfectly aligned with B, and thus does not give a rotation. It is important to note, however, that any discrete timelapse gives a ro-

Table 3.1: In the left column the constraint equations derived in Subsection 3.3.1 are found. Having four equations and four unknown parameters, it is possible to find unique solutions. These are found in the right column.

Constraints	Solutions
$1.63 \times 10^{-4} = \rho_{\mathrm{w}} \frac{2Nr_{\mathrm{c}}}{\beta^2}$	$N = 77$
$r_{\mathrm{w,min}} = \beta r_{\mathrm{b,min}}$	$r_{\mathrm{c}} = 5.81 \times 10^{-4}\,\mathsf{m}$
$r_{\mathrm{c}} = \frac{\sqrt{2}}{4} r_{\mathrm{b,min}}$	$\beta = 3.0 \times 10^{-3}$
$\frac{\sqrt{2}}{4} r_{\mathrm{b,min}} = 2Nr_{\mathrm{w,min}}$	$r_{\mathrm{b,min}} = 1.64 \times 10^{-3}\,\mathsf{m}$

tation, in which case $I_{\mathrm{eff},1}$ will have an effect. Therefore, to ensure sustained rotation around a single axis, this measure has to be taken to eliminate back-EMF.

With the three constraints shown in Equation 3.24, it is now possible to calculate the three unknown variables $[\omega_2, I_{\mathrm{in},1}, I_{\mathrm{in},3}]^T$.

The red line in Figure 3.2A shows the resulting ω_2 for $\mathsf{B} = 1.5\,\mathsf{T}$ and $\eta = 200\,\mathsf{mPa\,s}$. For decreasing r_{b}, ω_2 is seen to increase from $3.8\,\mathsf{rad\,s^{-1}}$ to $34\,\mathsf{rad\,s^{-1}}$. As seen in Equation 3.24 $\omega_2 \propto I_{\mathrm{eff},3}/r^3$. Since $I_{\mathrm{eff},3}$ is closely related to I_{tot}, it is closely related to ${r_{\mathrm{b}}}^2$ as well. The net result is that ω_2 is nearly proportional to $1/r_{\mathrm{b}}$.

3.3.3 Translational domain

In a previous study, Bernardo & Moraes (2011) found that P_{T} of a helix was divided by 12.5 when a spherical head was attached. Since that is the case in this study, that was taken into account. According to Equation 3.11, $v \propto \sqrt{P_{\mathrm{T}}}$, thus Equation 3.7 was adjusted to Equation 3.25.

$$v = \frac{\omega r_{\mathrm{t}}}{\sqrt{12.5}} \left(\frac{\sin(2\theta)}{3 - \cos(2\theta)} \right) = 5.4\,\mathsf{mm\,s^{-1}} \tag{3.25}$$

Using Equations 3.25 and 3.8 it is possible to calculate v and v_{rel} from ω_2. The results are shown as the blue line in Figure 3.2A and the black line in Figure 3.2B respectively. The tail was chosen to have the same radius as the capsule, i.e. $r_{\mathrm{t}} = r_{\mathrm{b}}$, $\theta = \pi/4$ rad [42] and $bl = 2r_{\mathrm{b}}$. Furthermore, Re can be seen as the red line in Figure 3.2B.

The v is seen to be relatively constant during downscaling, from $5.4\,\mathsf{mm\,s^{-1}}$ to $5.3\,\mathsf{mm\,s^{-1}}$. The small deviation seen at small r_{b}, is due to the increased ω_2, which in turn increased the back EMF and thus $I_{\mathrm{eff},2}$. The v_{rel} is seen to increase with a factor of 9 in downscaling, from $0.18\,\mathsf{s^{-1}}$ to $1.6\,\mathsf{s^{-1}}$. It can be concluded from the Re staying below 1, that the used equations of motion or applicable in this case.

It is important to note however, that η is 200 times higher than that of water [43] and approximately 50 times that of blood [44]. This is done to ensure low-Re, and it is an artificial way to simulate smaller bodies at lower velocities, even if their design does not permit them to be as small.

3.3.4 Power and efficiencies

In contrast to the relative swimming velocity of the UD, if r_{b} decreases, less current

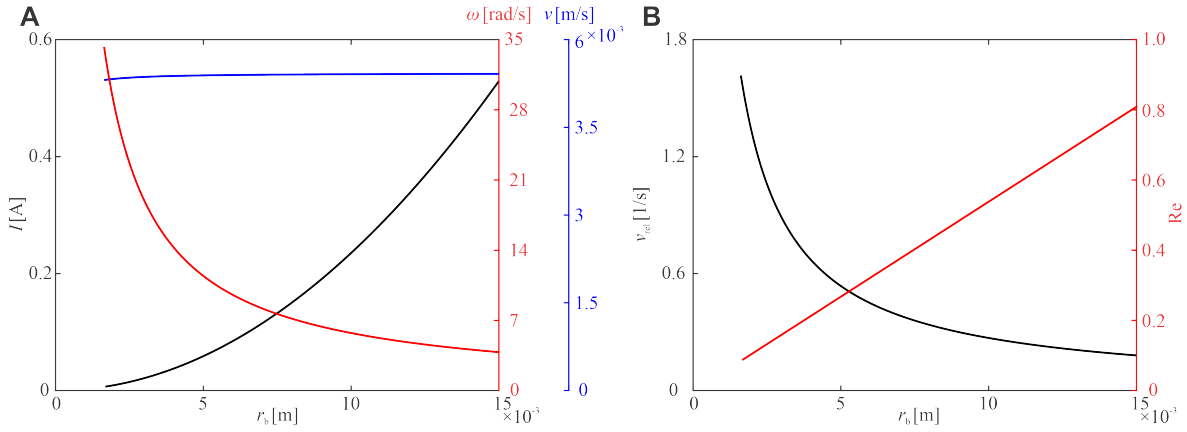

Figure 3.2: The total current drawn by on-board tri-axial electromagnetic coils, I_{tot}, angular velocity, ω_2, and translational speed, v, are calculated for different sizes of the untethered device (UD) in the $1.64\,\mathrm{mm} \leq r_{\mathrm{b}} \leq 15\,\mathrm{mm}$ *range. Parameters:* $B = 1.5\,\mathrm{T}$ *(within the range of a magnetic resonance imaging system),* $\eta = 200\,\mathrm{mPa\,s^{-1}}$, $\rho = 997\,\mathrm{kg\,m^{-3}}$. *(A) The current drawn by the tri-axial coils decreases as size decreases, from* $0.53\,\mathrm{A}$ *to* $6.3\,\mathrm{mA}$. *The angular velocity increases drastically by downscaling the UD, from* $3.8\,\mathrm{rad\,s^{-1}}$ *to* $34\,\mathrm{rad\,s^{-1}}$, *while the translational velocity only slightly decreases, from* $5.4\,\mathrm{mm\,s^{-1}}$ *to* $5.3\,\mathrm{mm\,s^{-1}}$. *(B) The relative velocity,* $v_{\mathrm{rel}} = v/(2r_{\mathrm{b}})$, *increases from* $0.18\,\mathrm{s^{-1}}$ *to* $1.6\,\mathrm{s^{-1}}$ *as the size of the UD decreases. Over the entire range of* r_{b}, *we have* $\mathrm{Re} < 1$.

can be generated. Following Equation 3.9, $P_{\mathrm{E}} \propto {r_{\mathrm{b}}}^2$, which is shown as the black line in Figure 3.3(A). The P_{R} and P_{T}, using Equations 3.10 and 3.11, are shown as the red and blue lines in Figure 3.3(A). Both decrease approximately linear with r_{b}, separated by a constant factor of 6.7×10^{-3}.

The η_{R} is shown as the solid black line in Figure 3.3B, increasing from $0.11\,\%$ to $0.98\,\%$ for decreasing r_{b}. Since this transduction of energy between the rotational and translational domain is constant, only η_{R} is shown as η_{T} shows the exact same relation with r_{b}. For the other graphs in Figure 3.3B, the field strength is varied through a wide range of $50 \times 10^{-6}\,\mathrm{T} \leq \mathrm{B} \leq 1.5\,\mathrm{T}$, where its lower limit represents earth's magnetic field and the upper limit that of a standard MRI field. It is unlikely that a UD can rotate using earth's magnetic field, given the very low η_{R}. However, the efficiency is much higher for a greater magnetic field for a given UD's size, as can be expected from Equation 3.24. Note that η_{R} (Figure 3.3(B)) and v_{rel} (Figure 3.2(B)) show a similar increase as r_{b} decreases.

3.3.5 Fuel consumptions

Using Equations 3.15, 3.16 and 3.17, the consumption rates of the three required substances are shown in Figure 3.4(A). In the proposed design, CaH_2 would be present in the capsule while H_2O is supplied from the surrounding bodily fluid. It is important to note that the molecular ratios between H_2O and H_2 in the hydrolysis reaction and in the current generation by the fuel cell are equal to each other. So the amount of H_2O needed is approximately the same as the amount of water produced. The O_2 required is not produced in the capsule, more on that in discus-

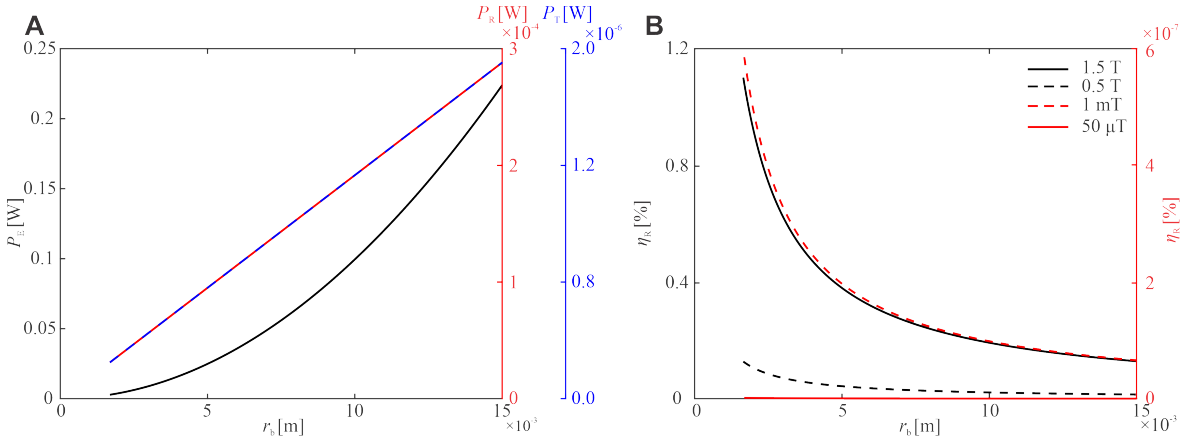

Figure 3.3: The size and the external magnetic field strength have a direct influence on the electrical power, P_E, rotational power, P_R, translational power P_T, and rotational efficiency, η_R. Parameters: $\eta = 200$ mPa s, $\rho = 997$ kg m^{-3}. (A) The P_E decreases quadratically with decreasing size, from 223 mW to 2.7 mW. The P_R and P_T both show a linear decrease, separated by a constant factor of 6.7×10^{-3}. (B) Regardless of the external magnetic field strength, the UD becomes more efficient as size decreases, with the highest η_R equal to 0.98 %.

sion. Since the fuel rates are linearly dependent on the current that is drawn, they show a quadratic relation with r_b.

The UD relies on multiple fuel sources, of which the storage of CaH_2 is limited by the size of the UD. Therefore the consumption rate will provide an estimate of its lifetime (t_l) as a function of r_b. The C_C decreases approximately quadratically as r_b decreases. Under the assumption that one hemisphere of the UD would be available for storage, this volume approximately decreases proportionally to ${r_b}^3$. Therefore the expected t_l decreases linearly with r_b, which can be found from Equation 3.26 and seen in Figure 3.4(B).

3.4 Conclusion

Table 3.2 provides a short summary of characteristics of the electrical, motion, and performance characteristics of three UDs, with an r_b of 1.64 mm, 9.0 mm, and 15 mm. The smallest has a t_l of 6.3 h, while the larger UDs have a t_l of 35 h and 58 h, respectively. The power density (P_d), shows a linear increase for decreasing r_b, since $P_E \sim {r_b}^2$ but the volume is proportional to ${r_b}^3$. These scaling rules present advantages in downscaling and are favourable for microrobots, especially the nearly constant v and even increasing v_{rel} are highly desirable. [24]

$$\text{Lifetime (s)} = \frac{2\pi r_b^3}{3C_C} \qquad (3.26)$$

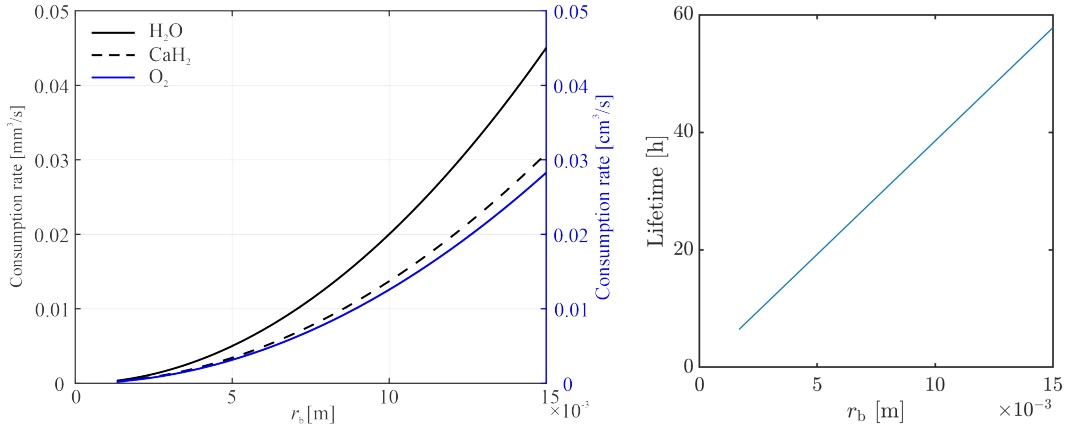

Figure 3.4: (A) The end-to-end process indicates the consumption rate of CaH_2/O_2 for the $1.64\,\mathrm{mm} \leq r_\mathrm{b} \leq 15\,\mathrm{mm}$ *range. The* $15\,\mathrm{mm}$ *UD consumes* $4.5 \times 10^{-2}\,\mathrm{mm^3\,s^{-1}}$ *of* H_2O *and* $3.0 \times 10^{-2}\,\mathrm{mm^3\,s^{-1}}$ *of* CaH_2*. The consumption of* O_2 *is* $2.9 \times 10^{-2}\,\mathrm{cm^3\,s^{-1}}$*. These rates decrease quadratically with size to respectively* $5.9 \times 10^{-4}\,\mathrm{mm^3\,s^{-1}}$*,* $4.1 \times 10^{-4}\,\mathrm{mm^3\,s^{-1}}$ *and* $3.7 \times 10^{-4}\,\mathrm{cm^3\,s^{-1}}$ *at a radius of* $1.64\,\mathrm{mm}$*. (B) Expected lifetime of the UD as a function of* r_b*. At an* r_b *of* $15\,\mathrm{mm}$*, the lifetime is* $58\,\mathrm{h}$*. It is seen to linearly decrease for decreasing* r_b*, to* $6.3\,\mathrm{h}$ *at an* r_b *of* $1.64\,\mathrm{mm}$*.*

Table 3.2: The electrical and swimming characteristics of an untethered device (UD) are calculated for three sizes. Hydrodynamic efficiencies, power and energy density, fuel consumption rate, and lifetime of each UD of body length, bl, are calculated for an external field of $1.5\,\mathrm{T}$ *and fluid with viscosity of* $200\,\mathrm{mPa\,s}$*. The consumption rate of the hydrogen source and lifetime are* C_C *and* t_l*, respectively. The UD of* $1.64\,\mathrm{mm}$ *radius is important for microrobotic applications while a UD of* $15\,\mathrm{mm}$ *diameter is relevant for active capsule endoscopes.*

r_b [mm]	I [A]	ω_2 [rad s^{-1}]	v [mm s^{-1}]	v_rel [s^{-1}]	Re	P_d [mW mm^{-3}]	η_R [%]	η_T [%]	C_C [mm^3 s^{-1}]	t_l [h]
1.64	6.3×10^{-3}	34	5.3	1.6	0.087	0.29	0.98	6.5×10^{-3}	4.1×10^{-4}	6.3
9.0	0.19	6.4	5.4	0.30	0.49	5.3×10^{-2}	0.18	1.2×10^{-3}	1.1×10^{-2}	35
15	0.53	3.8	5.4	0.18	0.81	3.2×10^{-2}	0.11	7.4×10^{-4}	3.0×10^{-2}	58

Chapter 4

Discussion

In Section 4.1 the results of Section 3.3 are extrapolated towards smaller values of r_b. In Section 4.2 the shortcomings encountered in this study will be presented, while in Section 4.3 limitations inherent to this design are shown.

4.1 Extrapolation

In the modelling used in Section 3.3, the geometry of the UD is used to determine the $r_{\mathrm{b,min}}$ for which the tri-axial coils can still be fit in the capsule. In this section, these results are extrapolated, under the assumption that the constraint on the size of the UD is let go. To avoid divisions by zero, the arbitrary value for the smallest r_b is chosen as $1\,\mu\mathrm{m}$.

Most of the results, such as the I_tot, the $\boldsymbol{\omega}$ and the consumption rates, continue the expected trends discussed in Section 3.3. Two of these results, however, give interesting insights into downscaling beyond $r_{\mathrm{b,min}}$. The first is the v, which is seen in Figure 4.1(A). Unlike the small decrease in Figure 3.2(A), it can be seen that v actually approaches $0\,\mathrm{mm\,s^{-1}}$ when lower values of r_b are considered. Although this differs from the results in Section 3.3, this can be expected considering the $\boldsymbol{\omega}$ continues to rise when r_b decreases. Therefore, the current which negates the back-EMF increases as well.

In Figure 4.1(B) the η_R can be seen for both $\boldsymbol{B} = 0.5\,\mathrm{T}$ and $\boldsymbol{B} = 1.5\,\mathrm{T}$. In Figure 3.3(B), the η_R was seen to keep increasing for decreasing r_b. For smaller r_b a peak at $11.3\,\%$ can be seen for both values of $\boldsymbol{B}$. That can be explained with similar reasoning as for the v: the P_R keeps increasing due to an increasing $\boldsymbol{\omega}$, but the same holds for the back-EMF. The peaks in Figure 4.1(B) demonstrate the r_b where this trade-off occurs. If $\boldsymbol{B}$ is smaller, the back-EMF is as well, which explains why for $\boldsymbol{B} = 0.5\,\mathrm{T}$ the peak is shifted to the left with respect to the graph of $\boldsymbol{B} = 1.5\,\mathrm{T}$. The graphs of $\boldsymbol{B} = 1\,\mathrm{mT}$ and $50\,\mu\mathrm{T}$ show an equal η_R and shift in location, but since their peaks are located at very low values of r_b, respectively $1.6 \times 10^{-11}\,\mathrm{m}$ and $4.1 \times 10^{-14}\,\mathrm{m}$, they are not shown here.

In conclusion, if a design for this type of UD would be proposed that has a lower limit on the size, if r_b becomes small enough, the v will decrease, which is characterized by an η_R that will stop increasing.

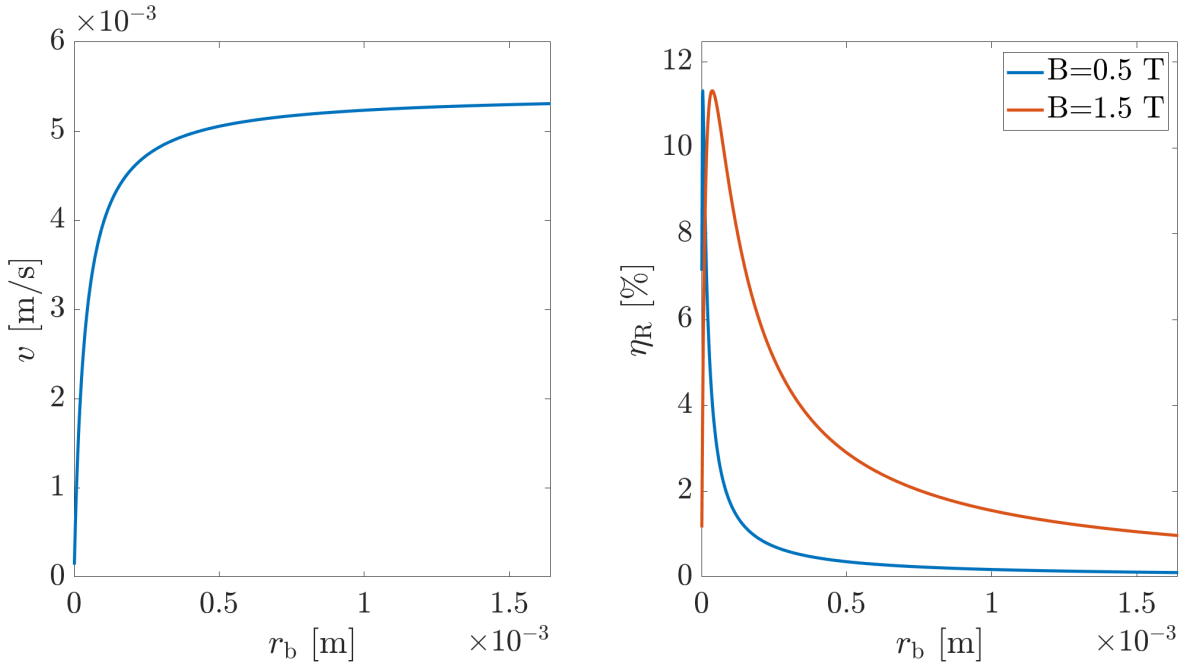

Figure 4.1: Here the altered dynamics of the capsule are shown, in case the lower limit on r_b is let go. The chosen range for r_b is $1\,\mu\mathrm{m} \leq r_\mathrm{b} \leq 1.65\,\mathrm{mm}$. (A) Here v is shown as a function of r_b. The v is $5.3\,\mathrm{mm\,s^{-1}}$ near $r_{\mathrm{b,min}}$, but instead of the small decrease seen in Figure 3.2(A), v plummets to $0.14\,\mathrm{mm\,s^{-1}}$ at $r_\mathrm{b} = 1\,\mu\mathrm{m}$. (B) Here the η_R is shown as a function of r_b, for $\boldsymbol{B} = 0.5\,\mathrm{T}$ in blue and for $\boldsymbol{B} = 1.5\,\mathrm{T}$ in red. Instead of the continuing rise seen in Figure 3.3(B), the η_R shows a peak at small r_b. For both values of $\boldsymbol{B}$ this peak is at $11.3\,\%$, in the case of $0.5\,\mathrm{T}$ at $r_\mathrm{b} = 4.12\,\mu\mathrm{m}$ and for $1.5\,\mathrm{T}$ at $r_\mathrm{b} = 37.0\,\mu\mathrm{m}$.

4.2 Shortcomings of this study

The experiments performed for this study were on the parametrization of a single PEMFC, with which a polarization curve can be modelled. Although this model has been built around physical parameters, the theorized effect of scaling on these parameters has not been experimentally validated. It has proven difficult and time-consuming to establish a set of fuel cells of different sizes with the same properties and materials. Therefore the relationships proposed in Table 2.1 are, as of yet, not certain. The same holds for the subsequent relationship between the current at peak power and the size of the UD.

The mechanical modelling of the capsule also has not been experimentally validated. The reason behind this is the complexity that arises from building such a capsule across different branches of science, incorporating chemical processes, an electrical circuit and subsequent locomotion. The electro-mechanical modelling of this capsule is based on various sources in literature, but this proposed design has not been built as of now. Experiments on this system are needed to justify this model, and only after validation can it be used in the next steps of development.

Furthermore, in the hydromechanical modelling of the capsule, $\boldsymbol{\omega}$ was found from a torque balance in which the body was assumed to be a sphere without a tail. In practice, however, the torque balance should include the tail as well. It proved impossible to include a helical tail in an analytical model, without using a finite element method. Including this will most likely not alter the results significantly, since the size of the tail is assumed to be proportional to r_b. Only a small decrease in $\boldsymbol{\omega}$, and thus v, is expected.

The model used to calculate the v, assumes that $\mathrm{Re}<1$. Especially for the final design in mind, where microbots would be inserted into the human body, this should hold. To comply with this, the η of the fluid was artificially set at $200\,\mathrm{mPa\,s}$, instead of the viscosity of blood, which is approximately $4\,\mathrm{mPa\,s}$ [44]. For the first set of experiments, this increased viscosity can still be used to comply with the condition of low-Re. However, in the future, a smaller design would be needed to ensure low-Re even in fluids with a viscosity similar to that of blood or other bodily fluids.

The next point that will be discussed has to do with the calculation of the t_l. It is assumed that the reaction kinetics of the hydrolysis of CaH_2 remain constant over time. However, the more of the CaH_2 has reacted, the more $Ca(OH)_2$ is formed. Over time, this leads to increased difficulties for the water to react with CaH_2, and thus less generation of hydrogen. [18] To investigate the slowing down of this reaction further experiments are needed that incorporate both the generation of hydrogen and the subsequent generation of electricity.

The final point to be discussed is regarding the temperature in the experiments. For this, the room temperature was used as the temperature of the fuel cell. However, any flow of energy, in this case in the form of electricity and chemical reactions, affects the temperature. And following Equation 2.17, a change in temperature leads to a change in

output voltage. Therefore, more detailed experiments should include temperature measurements, to find a relationship between current and temperature, so Equation 2.17 can be used more accurately.

4.3 Limitations of the chosen design

The first limitation worth mentioning is the deterioration of the fuel cell over time. This is demonstrated in Figure 4.2, where the voltage losses are much higher in the final measurements than in the initial measurements. This is shown further in Table 4.1, especially the I_0, R_O and I_L show a definitive deterioration. This is in line with the literature, where, among others, degradation of the catalyst, membrane and mass transfer have been reported [45]. This affected the study by decreasing the operating range of the fuel cell. Where it first was able to generate currents near $1.5\,\mathrm{A}$, this changed to $1\,\mathrm{A}$. Due to the fixed step size in the battery charger used in this study, the amount of data points has decreased in the final measurements. This has made the optimization procedure more uncertain. Since this decreases the reproducibility of fuel cells, this deterioration over time has to be taken into account for future studies.

The second limitation has to do with the type of fuell cell used in this study, i.e. a PEMFC. As stated earlier, this type needs both hydrogen and oxygen for the generation of electricity. In literature, multiple ways of generating hydrogen were given, of which the hydrolysis of CaH_2 was chosen in this

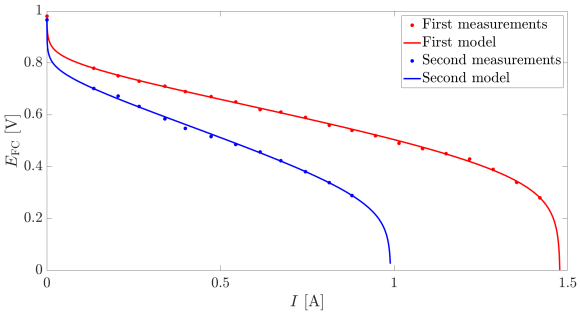

Figure 4.2: In red the first measurements of the fuel cell can be seen together with the fitted model. In blue the measurements and fitted model of the same fuel are found, only several months later. From this figure, it is clear that the internal dynamics of the fuel cell have deteriorated. The voltage losses have increased drastically in the final measurements, which can be seen as a shift towards the left.

study. However, for oxygen, such a thing was not found. Therefore, keeping in mind the intended *in vivo* use, this type of fuel cell will most likely not be used in the final design of such a capsule. The model proposed in this study is still helpful in modelling any capsule powered by a fuel cell, but another type has to be found that bypasses the use of oxygen. One that is promising in a biological setting is the so-called microbial fuel

Table 4.1: In the second column the initial values of the experimental parameters are shown. In the third column, the final values are given. From the decrease in I_0 and I_L, and from the increase of R_O it can be clearly seen that the dynamics of the PEMFC have deteriorated.

Parameter	Initial value	Final value
I_0 (A)	1.60×10^{-4}	3.43×10^{-5}
R_O (Ω)	0.18	0.35
c ($\mathrm{V\,K^{-1}}$)	2.26×10^{-4}	1.78×10^{-4}
I_L (A)	1.48	0.99
V_{H_2} (V)	0.25	0.26

cell. Instead of anorganic substances, it has been proven that certain types of microbial fuel cell are able to generate electrical energy from organic substances found connected to the human body. [46] Such a type of fuel cell could theoretically be used to power a UD similar to the one proposed in this study.

Chapter 5

Conclusions and recommendations

In Section 5.1 the conclusions of this study will be stated, while in Section 5.2 the recommendations for future studies building on this are given.

5.1 Conclusions

Based on the combined modelling of the proton exchange membrane fuel cell and the design and modelling of the untethered device, the following research question can be answered:

How are swimming velocity and fuel consumption of an untethered device with full energetic autonomy affected when scaling down?

The swimming velocity of the capsule is almost constant at $5.4\,\mathrm{mm\,s^{-1}}$, with a minimal decrease at the smallest radius. Over the entire range of radii, the relative velocity is another useful description. In scaling down, this is approximately proportional to the inverse of the radius, with a maximum of $1.6\,\mathrm{s^{-1}}$ in a UD at a radius of $1.64\,\mathrm{mm}$.

To answer the second part of the question, the fuel consumption for hydrogen, oxygen and water have a quadratic relationship with the radius. Since the size of the fuel reservoir decreases cubically, the lifetime of such a capsule decreases linearly with the radius, from $58\,\mathrm{h}$ to $6.3\,\mathrm{h}$.

5.2 Recommendations

In this study, the relationship between the five parameters of the fuel cell and r_b has been theoretically addressed. A future study needs to be done in which experiments are performed on fuel cells of different sizes. That way the theoretical relationship between the parameters and the r_b can be experimentally validated.

Secondly, the end-to-end model starting at a chemical fuel and ending at propulsion needs to be experimentally validated. On the one hand, the generation of hydrogen and subsequently electrical current should be tested against the model proposed in this study. On the other hand, a capsule similar to this design, only with a built-in battery, should be fabricated with which the maximum propulsion velocity should be tested. Once those are sufficiently understood, and if necessary the model has been changed accordingly, a complete prototype needs to be made so the complete end-to-end relationship from electrochemistry to hydrodynamics can be experimentally validated.

Finally, the PEMFC is the most common and understood type of fuel cell. For this study, hydrogen can be generated with straightforward hydrolysis. However, this is not the case for the other fuel, i.e. oxygen. With the final goal of use *in vivo* in mind, fuel cells more compatible with biological systems should be researched for this purpose, such as microbial fuel cells.

Bibliography

[1] E. M. Purcell, "Life at low reynolds number," *American Journal of Physics*, vol. 45, no. 2, pp. 3–11, 1977.

[2] M. Sitti, "Voyage of the microrobots," *Nature*, vol. 458, p. 1121–1122, 2009.

[3] B. J. Nelson, I. K. Kaliakatsos, and J. J. Abbott, "Microrobots for minimally invasive medicine," *Annual Review of Biomedical Engineering*, vol. 12, no. 1, pp. 55–85, 2010.

[4] R. Feynman, "There is plenty of room at the bottom. california institute of technology," *Int. J. Eng. Sci*, vol. 4, pp. 23–36, 1960.

[5] A. Darzi and Y. Munz, "The impact of minimally invasive surgical techniques," *Annual Review of Medicine*, vol. 55, no. 1, pp. 223–237, 2004, pMID: 14746519.

[6] K. D. Robertson and R. Singh, "Capsule endoscopy," in *StatPearls*. Treasure Island (FL): StatPearls Publishing, Jan. 2023.

[7] G. Ciuti, A. Menciassi, and P. Dario, "Capsule endoscopy: From current achievements to open challenges," *IEEE Reviews in Biomedical Engineering*, vol. 4, pp. 59–72, 2011.

[8] J. Mathieu, G. Soulez, and S. Martel, "Potential applications of untethered microdevices in the blood vessels within the constraints of an mri system," in *2005 IEEE Engineering in Medicine and Biology 27th Annual Conference*. IEEE, 2006, pp. 4850–4853.

[9] P. Swain, "The future of wireless capsule endoscopy," *World journal of gastroenterology: WJG*, vol. 14, no. 26, p. 4142, 2008.

[10] M. Rasouli and L. S. J. Phee, "Energy sources and their development for application in medical devices," *Expert review of medical devices*, vol. 7, no. 5, pp. 693–709, 2010.

[11] S. Martel, M. Mohammadi, O. Felfoul, Z. Lu, and P. Pouponneau, "Flagellated magnetotactic bacteria as controlled mri-trackable propulsion and steering systems for medical nanorobots operating in the human microvasculature," *The International Journal of Robotics Research*, vol. 28, no. 4, pp. 571–582, 2009, pMID: 19890435. [Online]. Available: https://doi.org/10.1177/0278364908100924

[12] X. Li, H. Zhang, F. Peng, Y. Li, T. Yang, B. Wang, and D. Fang, "A wireless magnetic resonance energy

transfer system for micro implantable medical sensors," *Sensors*, vol. 12, no. 8, pp. 10 292–10 308, 2012. [Online]. Available: https://www.mdpi.com/1424-8220/12/8/10292

[13] E. Steager, C.-B. Kim, J. Patel, S. Bith, C. Naik, L. Reber, and M. J. Kim, "Control of microfabricated structures powered by flagellated bacteria using phototaxis," *Applied Physics Letters*, vol. 90, pp. 263 901 – 263 901, 07 2007.

[14] C. Lozano, B. Hagen, H. Löwen, and C. Bechinger, "Phototaxis of synthetic microswimmers in optical landscapes," *Nature Communications*, vol. 7, p. 12828, 09 2016.

[15] P. Jin, J. Fu, F. Wang, Y. Zhang, P. Wang, X. Liu, Y. Jiao, H. Li, Y. Chen, Y. Ma, and X. Feng, "A flexible, stretchable system for simultaneous acoustic energy transfer and communication," *Science Advances*, vol. 7, no. 40, p. eabg2507, 2021. [Online]. Available: https://www.science.org/doi/abs/10.1126/sciadv.abg2507

[16] A. Kirubakaran, S. Jain, and R. Nema, "A review on fuel cell technologies and power electronic interface," *Renewable and Sustainable Energy Reviews*, vol. 13, no. 9, pp. 2430–2440, 2009.

[17] R. Henne and K. Friedrich, "Applications – transportation — auxiliary power units: Fuel cells," in *Encyclopedia of Electrochemical Power Sources*, J. Garche, Ed. Amsterdam: Elsevier, 2009, pp. 157–173.

[18] V. Vilasur Swaminathan, L. Zhu, B. Gurau, R. Masel, and M. Shannon, "Integrated micro fuel cell with on-demand hydrogen production and passive control mems," *Microfluidics and Nanofluidics*, vol. 12, 03 2011.

[19] T. Kim, "Fully-integrated micro pem fuel cell system with nabh4 hydrogen generator," *International Journal of Hydrogen Energy*, vol. 37, no. 3, pp. 2440–2446, 2012, 2010 AIChE Annual Meeting Topical Conference on Hydrogen Production and Storage Special Issue. [Online]. Available: https://www.sciencedirect.com/science/article/pii/S0360319911024207

[20] A. Balakrishnan, M. Frei, S. Kerzenmacher, H. Reinecke, and C. Müller, "Design and fabrication of miniaturized pem fuel cell combined microreactor with self-regulated hydrogen mechanism," *Journal of Physics: Conference Series*, vol. 660, p. 012055, 12 2015.

[21] T. Maiyalagan and S. Pasupathi, "Components for pem fuel cells: an overview," in *Materials science forum*, vol. 657. Trans Tech Publ, 2010, pp. 143–189.

[22] A. Hanna, K. S. Loh, W. Wong, R. Mohamad Yunus, T. K. Lee, A. Ahmad, and S. Chong, "Review of chitosan-based polymers as proton exchange membranes and roles of chitosan-supported ionic liquids," *International Journal of Molecular Sciences*, vol. 21, p. 632, 01 2020.

[23] C. Hartnig and C. Roth, *Fundamentals and Performance of Low Temperature Fuel Cells*, ser. Polymer electrolyte membrane and direct methanol fuel cell technology. Woodhead Publishing, 2012, vol. 1.

[24] E. van Renselaar, B. Keitel, M. Dinc, B. Mizaikoff, A. Susarrey-Arce, H. J. G. E. Gardeniers, L. Abelmann, and I. S. M. Khalil, "Scaling rules for microrobots with full energetic autonomy," in *2022 International Conference on Manipulation, Automation and Robotics at Small Scales (MARSS)*, 2022, pp. 1–6.

[25] A. J. Bard, R. Parsons, and J. Jordan, *Standard potentials in aqueous solution*. Taylor & Francis Inc, 1 1985. [Online]. Available: https://www.osti.gov/biblio/5826063

[26] Z. Li, Z. Zheng, L. Xu, and X. Lu, "A review of the applications of fuel cells in microgrids: opportunities and challenges," *BMC Energy*, vol. 1, no. 1, p. 8, Oct 2019. [Online]. Available: https://doi.org/10.1186/s42500-019-0008-3

[27] K. Kinoshita and P. Stonehart, *Modern Aspects of Electrochemistry*. New York: Plenum Press, 1977, ch. 4.

[28] A. Samris, H. Mounir, and A. E. Marjani, "Effect of platinum dispersity, platinum loading and pt-oxide coverage on oxygen reduction reaction in pemfc-cathode," *Journal of Electroanalytical Chemistry*, vol. 895, p. 115414, 2021. [Online]. Available: https://www.sciencedirect.com/science/article/pii/S1572665721004409

[29] M. Uchimura and S. Kocha, "The impact of cycle profile on pemfc durability," *ECS Transactions*, vol. 11, pp. 1215–1226, 09 2007.

[30] O. Holton and J. Stevenson, "The role of platinum in proton exchange membrane fuel cells," *Platinum Metals Review*, vol. 57, pp. 259–271, 10 2013.

[31] S. Bergens and M. Markiewicz, *FUEL CELLS – PROTON-EXCHANGE MEMBRANE FUEL CELLS — Cathodes*, J. Garche, Ed. Amsterdam: Elsevier, 2009. [Online]. Available: https://www.sciencedirect.com/science/article/pii/B9780444527455002240

[32] F. Barbir, "Chapter three - fuel cell electrochemistry," in *PEM Fuel Cells (Second Edition)*, 2nd ed., F. Barbir, Ed. Boston: Academic Press, 2013, pp. 33–72. [Online]. Available: https://www.sciencedirect.com/science/article/pii/B9780123877109000035

[33] W. Wang, X. Wei, D. Choi, X. Lu, G. Yang, and C. Sun, "Chapter 1 - electrochemical cells for medium- and large-scale energy storage: fundamentals," in *Advances in Batteries for Medium and Large-Scale Energy Storage*, ser. Woodhead Publishing Series in Energy, C. Menictas, M. Skyllas-Kazacos, and T. M. Lim, Eds. Woodhead Publishing, 2015, pp. 3–28. [Online]. Available: https://www.sciencedirect.com/science/article/pii/B9781782420132000017

[34] S. Li, X. Wei, H. Dai, H. Yuan, and P. Ming, "Voltammetric and galvanostatic methods for measuring hydrogen crossover in fuel cell," *iScience*, vol. 25, no. 1, p. 103576, 2022. [Online]. Available: https://www.sciencedirect.com/science/article/pii/S2589004221015467

[35] L. W. Juang, P. J. Kollmeyer, T. M. Jahns, and R. D. Lorenz, "Improved nonlinear model for electrode voltage-current relationship for more consistent online battery system identification," in *IEEE Energy Conversion Congress and Exposition*, 2011, p. 2628–2634.

[36] C. Spiegel, *PEM fuel cell modeling and simulation using matlab*. Massachussets: Academic Press, 2008.

[37] S. Puranik, A. Keyhani, and F. Khorrami, "State-space modeling of proton exchange membrane fuel cell," *Energy Conversion, IEEE Transactions on*, vol. 25, pp. 804 – 813, 10 2010.

[38] U. Chakraborty, "Fuel crossover and internal current in proton exchange membrane fuel cell modeling," *Applied Energy*, vol. 163, pp. 60–62, Feb. 2016.

[39] P. C. Ellgen, *Thermodynamics and Chemical Equilibrium*, 1st ed. CreateSpace Independent Publishing Platform, 2014.

[40] M. Schoemaker, U. Misz, P. Beckhaus, and A. Heinzel, "Evaluation of hydrogen crossover through fuel cell membranes," *Fuel Cells*, vol. 14, 06 2014.

[41] L. D. Landau and E. M. Lifshitz, *Fluid Mechanics, Second Edition: Volume 6 (Course of Theoretical Physics)*, 2nd ed., ser. Course of theoretical physics / by L. D. Landau and E. M. Lifshitz, Vol. 6. Butterworth-Heinemann, 1987.

[42] B. de Lima Bernardo and F. Moraes, "Simplified model for the dynamics of a helical flagellum," *American Journal of Physics*, vol. 79, no. 7, p. 736–740, 2011.

[43] L. Korson, W. Drost-Hansen, and F. J. Millero, "Viscosity of water at various temperatures," *The Journal of Physical Chemistry*, vol. 73, no. 1, pp. 34–39, Jan 1969. [Online]. Available: https://doi.org/10.1021/j100721a006

[44] E. Nader, S. Skinner, M. Romana, R. Fort, N. Lemonne, N. Guillot, A. Gauthier, C. Renoux, E. Stauffer, P. Joly, Y. Bertrand, and P. Connes, "Blood rheology: Key parameters, impact on blood flow, role in sickle cell disease and effects of exercise," *Frontiers in Physiology*, vol. 10, 2019.

[45] P. Ren, P. Pei, Y. Li, Z. Wu, D. Chen, and S. Huang, "Degradation mechanisms of proton exchange membrane fuel cell under typical automotive operating conditions," *Progress in Energy and Combustion Science*, vol. 80, p. 100859, 2020. [Online]. Available: https://www.sciencedirect.com/science/article/pii/S0360128520300691

[46] D. Pankratov, L. Ohlsson, P. Gudmundsson, S. Halak, L. Ljunggren, Z. Blum, and S. Shleev, "Ex vivo electric power generation in human blood using an enzymatic fuel cell in a vein replica," *RSC Adv.*, vol. 6, pp. 70 215–70 220, 2016. [Online]. Available: http://dx.doi.org/10.1039/C6RA17122B

Appendix A

Back-EMF

According to Lenz's law, back-EMF can be calculated using Equation A.1,

$$EMF = -N\frac{\Delta\Phi}{\Delta t}, \tag{A.1}$$

with EMF the back-EMF, N the number of coils and Φ the magnetic flux through the coil. Consequently, the equation for Φ can be found in Equation A.2,

$$\Phi = BS\cos(\phi), \tag{A.2}$$

with B the magnetic field strength, S the surface area of the coil and ϕ the angle of the cross-section of the coil with respect to the magnetic field (0 rad is perpendicular).

It is important to note that for every full cycle ϕ makes, the coil is perpendical to B twice. Therefore, the time derivative of Φ has to be multiplied with a factor 2, leading to Equation A.3,

$$\frac{\Delta\Phi}{\Delta t} = -2BS\sin(\phi)\dot{\phi}, \tag{A.3}$$

with $\dot{\phi}$ the time derivative of ϕ. Then the current generated by the back-EMF (I_{EMF}) can be seen in Equation A.4,

$$I_{\mathrm{EMF}} = \frac{EMF}{R_{\mathrm{w}}} = \frac{2NBS\sin(\phi)\dot{\phi}}{R_{\mathrm{w}}}, \tag{A.4}$$

with R_{w} the resistance of the wire.